A&A 469, 27–46 (2007)
DOI: 10.1051/0004-6361:20066271

Astronomy & Astrophysics

The XMM-Newton serendipitous survey⋆,⋆⋆,⋆⋆⋆

III. The AXIS X-ray source counts and angular clustering

F. J. Carrera[1], J. Ebrero[1], S. Mateos[1,3], M. T. Ceballos[1], A. Corral[1], X. Barcons[1], M. J. Page[2], S. R. Rosen[2,3], M. G. Watson[3], J. A. Tedds[3], R. Della Ceca[4], T. Maccacaro[4], H. Brunner[5], M. Freyberg[5], G. Lamer[6], F. E. Bauer[7], and Y. Ueda[8]

[1] Instituto de Física de Cantabria (CSIC-UC), Avenida de los Castros, 39005 Santander, Spain
e-mail: carreraf@ifca.unican.es
[2] Mullard Space Science Laboratory, University College London, Holmbury St. Mary, Dorking, Surrey, RH5 6NT, UK
[3] Department of Physics and Astronomy, University of Leicester, Leicester, LE1 7RH, UK
[4] Osservatorio Astronomico di Brera, via Brera 28, 20121 Milano, Italy
[5] Max-Planck-Institut für extraterrestrische Physik, Postfach 1312, 85741 Garching, Germany
[6] Astrophysikalisches Institut Potsdam, An der Sternwarte 16, 14482 Potsdam, Germany
[7] Columbia Astrophysics Laboratory, Columbia University, Pupin Laboratories, 550 West 120th Street, Room 1418, New York, NY 10027, USA
[8] Department of Astronomy, Kyoto University, Kyoto 606-8502, Japan

Received 18 August 2006 / Accepted 9 March 2007

ABSTRACT

Context. Recent results have revised upwards the total X-ray background (XRB) intensity below ∼10 keV, therefore an accurate determination of the source counts is needed. There are also contradictory results on the clustering of X-ray selected sources.
Aims. We have studied the X-ray source counts in four energy bands: soft (0.5–2 keV), hard (2–10 keV), XID (0.5–4.5 keV) and ultra-hard (4.5–7.5 keV) in order to evaluate the contribution of sources at different fluxes to the X-ray background. We have also studied the angular clustering of X-ray sources in those bands.
Methods. AXIS (An *XMM-Newton* International Survey) is a survey of 36 high Galactic latitude *XMM-Newton* observations covering 4.8 deg^2 in the Northern sky and containing 1433 serendipitous X-ray sources detected with 5-σ significance. This survey has similar depth to the *XMM-Newton* catalogues and therefore serves as a pathfinder to explore their possibilities. We have combined this survey with shallower and deeper surveys, and fitted the source counts with a Maximum Likelihood technique. Using only AXIS sources we have studied the angular correlation using a novel robust technique.
Results. Our source counts results are compatible with most previous samples in the soft, XID, ultra-hard and hard bands. We have improved on previous results in the hard band. The fractions of the XRB resolved in the surveys used in this work are 87%, 85%, 60% and 25% in the soft, hard, XID and ultra-hard bands, respectively. Extrapolation of our source counts to zero flux is not sufficient to saturate the XRB intensity. Only galaxies and/or absorbed AGN could contribute the remaining unresolved XRB intensity. Our results are compatible, within the errors, with recent revisions of the XRB intensity in the soft and hard bands. The maximum fractional contribution to the XRB comes from fluxes within about a decade of the break in the source counts (∼10^{-14} cgs), reaching ∼50% of the total in the soft and hard bands. Angular clustering (widely distributed over the sky and not confined to a few deep fields) is detected at 99–99.9% significance in the soft and XID bands, with no detection in the hard and ultra-hard band (probably due to the smaller number of sources). We cannot confirm the detection of significantly stronger clustering in the hard-spectrum hard sources.
Conclusions. Medium depth surveys such as AXIS are essential to determine the evolution of the X-ray emission in the Universe below 10 keV.

Key words. surveys – X-rays: general – cosmology: large-scale structure of Universe

1. Introduction

The X-ray background (Giacconi et al. 1962) records the history of accretion power in the Universe (Fabian & Iwasawa 1999; Sołtan 1982), and as such its sources and their evolution have attracted considerable attention (Fabian & Barcons 1992). Deep pencil-beam surveys (Loaring et al. 2005; Bauer et al. 2004; Cowie et al. 2002; Giacconi et al. 2002; Hasinger et al. 2001) have resolved most (≳90%) of the soft (0.5–2 keV) XRB into individual sources. Most of these turn out to be unobscured and obscured Active Galactic Nuclei (AGN), while at the fainter fluxes a population of "normal" galaxies starts to contribute significantly to the source counts (Hornschemeier et al. 2003). At higher energies the resolved fraction is smaller (Worsley et al. 2004): 50% between 4.5 and 7.5 keV, and less than 50% between 7.5 keV and 10 keV. Models for the XRB based on the Unified Model for AGN successfully reproduce its spectrum with a combination of unobscured and obscured AGN, the latter being the

⋆ Table 1 and Appendices are only available in electronic form at http://www.aanda.org

⋆⋆ Based on observations obtained with XMM-newton, an ESA science mission with instruments and contributions funded by ESA Member States and the USA (NASA).

⋆⋆⋆ Tables 2 and 3 are only available in electronic form at the CDS via anonymous ftp to cdsarc.u-strasbg.fr (130.79.128.5) or via http://cdsweb.u-strasbg.fr/cgi-bin/qcat?J/A+A/469/27

dominant population (Setti & Woltjer 1989; Gilli et al. 2001). Recent hard X-ray AGN luminosity function results (Ueda et al. 2003; La Franca et al. 2005) show that such simple models need considerable revision, with a lower absorbed AGN fraction at higher luminosities and luminosity dependent density evolution of the hard X-ray AGN luminosity.

The fainter sources from deep surveys do not contribute much to the final XRB intensity and are often too faint optically and in X-rays to be studied individually. Stacking X-ray spectra is a valuable technique in these circumstances (Worsley et al. 2006; Civano et al. 2005), but only average properties can be deduced and this method does not account for the diversity in the nature of the sources necessary to account for the XRB. Wide shallow surveys over a large portion of the sky (Schwope et al. 2000; Della Ceca et al. 2004; Ueda et al. 2003) detect minority populations and allow studies of sources on an individual basis while serving as a framework against which to study and detect evolution, but again with only a minor contribution to the XRB.

Medium depth wide-band surveys combining many sources with relatively wide sky coverage (Hasinger et al. 2007; Pierre et al. 2004; Barcons et al. 2002; Baldi et al. 2002) have the potential to provide many of the missing pieces of the XRB/AGN puzzle, since most (30–50%) of the XRB below 10 keV comes from sources at intermediate fluxes (Fabian & Barcons 1992; Barcons et al. 2006), and the optical and X-ray spectra of many sources can be studied individually (e.g. Mateos et al. 2005). Furthermore, extensive *XMM-Newton* source catalogues are available (1XMM[1] -SSC 2003-), and significantly larger ones will become available in the near future (2XMM,...), which, since they are constructed from serendipitous sources in typical public *XMM-Newton* observations, are themselves medium flux surveys. The exploitation of the full potential of these catalogues depends on the results from "conventional" smaller scale, medium flux surveys such as those above and the one presented here.

Since AGN are the dominant population at medium and low X-ray fluxes, and X-ray selected AGN are known to cluster strongly (Yang et al. 2006; Gilli et al. 2005; Mullis et al. 2004; Carrera et al. 1998), it is interesting to investigate the angular clustering of X-ray sources, which can be performed without resorting to expensive ground-based spectroscopy. Angular correlation can be translated into spatial clustering via Limber's equation (Peebles 1980), if the luminosity function of the populations involved is known from other surveys. Several studies have investigated the angular clustering in the soft and hard bands on scales ranging from tens or hundreds of arcsec to degrees, with varying success in the detection of signal. Angular clustering has been detected in the soft band (Gandhi et al. 2006; Basilakos et al. 2005; Akylas et al. 2000; Vikhlinin & Forman 1995) with different values of the clustering strength. Angular clustering in the hard band has evaded detection in some cases (Gandhi et al. 2006; Puccetti et al. 2006), but not in others (Yang et al. 2003; Basilakos et al. 2004) where clustering strengths are found to be marginally compatible with the observed spatial clustering of optical and X-ray AGN.

We present here a medium X-ray survey which includes 1433 serendipitous sources over 4.8 deg^2 of the northern sky: AXIS (An X-ray International Survey). This survey was undertaken under the auspices of the *XMM-Newton* Survey Science Centre[2] (SSC). In this paper we present the source catalogue (Sect. 2), overall X-ray spectral properties (Sect. 3), number counts (Sect. 4, where some other samples have also been used), fractional contribution to the XRB (Sect. 5) and angular clustering properties (Sect. 6). Overall results are summarised in Sect. 7. In a forthcoming paper (Barcons et al. 2007) we present the optical identifications of a subsample of AXIS, which we have called the *XMM-Newton* Medium Survey (XMS). A complementary medium sensitivity study of optically identified sources in the southern hemisphere is also in preparation (Tedds et al. 2007). In this paper we will use cgs as a shorthand for the cgs system units for the flux: erg cm^{-2} s^{-1}.

2. The X-ray data

2.1. Selection of fields

A total of 36 *XMM-Newton* observations were selected for optical follow-up of X-ray sources within the AXIS programme (see Table 1), with a preference for those that were public early in the mission (mid 2000), or part of the SSC Guaranteed Time Program. We selected fields having $|b| > 20^\circ$, total exposure time >15 ks, and excluding (optical and X-ray) bright or extended targets (except in two cases: A1837 and A399). After discarding the observing intervals within observations having high background rates, a few of the fields have final exposure times shorter than 15 ks. A few fields (some with shorter exposure times) were also included to expand the solid angle for bright X-ray sources. All of these fields have been used for the study of cosmic variance, the angular correlation function and the determination of $\log N - \log S$ in different bands.

27 of the original 36 *XMM-Newton* observations were selected for optical follow-up of medium flux X-ray sources. Two of those 27 fields (A2690 and MS2137) were later excluded from the main identification effort because their Declination was too low to observe them from Calar Alto (Spain) with airmass lower than 2. The sources in the remaining 25 fields were used to form flux-limited samples in the 0.5–2 keV, 2–10 keV, 0.5–4.5 keV bands and a non-flux-limited sample in the 4.5–7.5 keV band and these constitute the final XMS sample (see Barcons et al. 2007). These 25 fields are marked in Table 1.

2.2. Data processing and relation to 1XMM

The data used in our earlier follow-up efforts (see previous Section) were originally processed with very different versions of the SAS (Science Analysis System, Gabriel et al. 2004). The reprocessing for the 1XMM catalogue (SSC 2003) provided a much more homogeneous set of X-ray data. The Observation Data Files (ODF) were processed in the SSC Pipeline Processing System (PPS) facilities at Leicester with the same SAS version used for 1XMM (very similar to SAS version 5.3.3, see below for the difference), except for the field Mkn 205, which was processed with SAS version 5.3.3. PHL1092 is a special case since the original *XMM-Newton* observation was never reprocessed and instead we used a newer set of data from the *XMM-Newton* Science Archive, which was processed later with a different SAS version (5.4.0).

[1] The first *XMM-Newton* Serendipitous Source Catalogue (1XMM), released in 2003, contains source detections drawn from 585 *XMM-Newton* EPIC observations and a total of ~30 000 individual X-ray sources. The median 0.2–12 keV flux of the catalogue sources is $\sim 3 \times 10^{-14}$ cgs, with ~12% of them having fluxes below 10^{-14} cgs.

[2] The *XMM-Newton* Survey Science Centre is an international collaboration involving a consortium of 10 institutions appointed by ESA to help develop the software analysis system, to pipeline process all the *XMM-Newton* data, and to exploit the *XMM-Newton* serendipitous source detections, see `http://xmmssc-www.star.le.ac.uk`

The main difference between the versions of the SAS source detection task (`emldetect`) used for Mkn205 and the rest of the fields is the inclusion of the possibility of sources with negative count rates in the latter. Negative count rates in individual energy bands were allowed to avoid a bias in the total count rates of sources that were undetected in one or more energy bands. However, since this option caused numerical problems in some cases, the count rates were limited to values ≥ 0 in later versions of the pipeline. Since negative count rates are meaningless, we have set all the negative count rates to zero in what follows. The corresponding detection likelihoods have also been set to zero, ensuring that the presence of that source in that band does not improve the fit (see below for details).

The standard SAS products include X-ray source lists (created by `emldetect`) for each of the three EPIC cameras (MOS1, MOS2, Turner et al. 2001, and pn, Strüder et al. 2001), determined in five independent bands (1: 0.2–0.5 keV, 2: 0.5–2.0 keV, 3: 2.0–4.5 keV, 4: 4.5–7.5 keV, and 5: 7.5–12.0 keV). In addition, the source detection algorithm was run in the 0.5–4.5 keV (band 9), which we will call the XID band. Since EPIC pn has the highest sensitivity of the three cameras, we have used only pn source lists. We have not allowed for source extent when detecting the sources, and therefore all the sources in our survey are treated as point like.

The internal calibration of the source positions from the SAS is quite good (1.5 arcsec, Ehle et al. 2005), but there may be some systematic differences between the absolute X-ray source positions and optical reference frames. We have registered the X-ray source positions to the USNO-A2 reference frame field by field, using the SAS task `eposcorr`. This task shifts the X-ray reference frame to minimise the differences between the X-ray source positions and the positions of their optical counterparts in a given reference astrometric catalogue (USNO-A2 in our case). These corrected positions are given in Table 2. The average shift in absolute value in RA (Dec) was 1.3 (0.9) arcsec, and in all cases the shifts were under 3 arcsec. The average number of X-ray-USNO-A2 matches used to calculate the shifts was 28 (the minimum was 16 and the maximum 82). There were two fields for which this procedure failed (Mkn3 and A399), probably in the first case because one quarter of the pn chips were in counting mode, and in the second case two moderately strong extended sources are located in opposite corners of the field. We therefore used the original X-ray source positions for these two fields.

2.3. Source selection

In each detection band the source detection algorithm fits a portion of the image around the position of the candidate source, trying to match the Point Spread Function (PSF) shape to the photon distribution. In this process it uses the background map and the exposure map to fit a source count rate and 2D position. The typical size of this region is the 80% encircled energy radius, which corresponds to about 5 pixels on-axis and 7 pixels at 15 arcmin off-axis (we have used 4 arcsec pixels throughout). Sources closer than this distance away from the pn chip edges may have a worse determination of their positions and/or count rates. We have therefore excluded all sources closer than the 80% encircled energy radius (taking into account the off-axis angle) to any pn chip edges. A region (~12 pixels wide) on the readout (outer) edge of the pn chips is masked out on board the satellite (Ehle et al. 2005). We have considered this "effective" edge as the outer edge of each chip when defining our excluded regions.

We have visually inspected all X-ray images, excluding circular regions around bright targets, and other bright/extended sources in the images (see Table 1 for the sizes and positions of these regions). In a few images a bright band extending from the target to the pn chip reading edge was visible, due to the photons arriving at the detector while it was being read out (called the Out Of Time – OOT – region). We have excluded a rectangular region around the OOT region, whose width is also given in Table 1. In addition, sources affected by bright pixels/segments have been excluded as well as those which were obviously affected by the presence of nearby bright sources, or split by the chip gaps and not picked up by the above procedures.

In addition there were two sets of fields which partially overlapped: G133-69pos_2 and G133-69Pos_1 on the one hand and SDS-1b, SDS-2 and SDS-3 on the other. We have dealt with this by masking out the portion of the second (and third) field which overlap with the first field, in the order given above.

We have used the following bands in the analysis performed in this paper:

- soft: 0.5–2 keV, identical to the standard SAS band 2;
- hard: combining standard SAS bands 3, 4 and 5 and hence corresponding to counts in the 2 to ~12 keV range. However, we have calculated (and will quote) all hard fluxes in 2–10 keV;
- XID: 0.5–4.5 keV, identical to the SAS band 9;
- ultra-hard: 4.5–7.5 keV, identical to the standard SAS band 4.

The detection likelihood in the hard band (L_{345}) was obtained from the detection likelihoods in bands 3, 4 and 5 (L_3, L_4, and L_5 respectively) using $L_{345} = -\log(1 - Q(5/2, L'_3 + L'_4 + L'_5))$, where L'_i can be obtained from $L_i = -\log(1 - Q(3/2, L'_i))$ and $Q(a, x)$ is the incomplete gamma function (see `emldetect` documentation).

There were a total of 2560 accepted sources with an `emldetect` detection likelihood ≥ 10 (the default value) in at least one band. These are listed in Table 2 with their corrected X-ray positions and count rates in the standard SAS and XID bands.

The original unfiltered source lists are identical to the ones used by Mateos et al. (2005) in their study of the detailed spectral properties of medium flux X-ray sources for the fields common to both studies. They also used similar criteria for excluding sources close to the pn chip edges except in the case of the readout edge. The differences in the final accepted source lists arose for several reasons: Mateos et al. used sources close to pn chip gaps (which we have excluded) if they were far from chip gaps in the MOS detectors. They excluded from their spectral analysis the sources with a low number of counts. Finally, we have treated the sources close to the exclusion zone boundaries slightly differently. These differences are at the 10% level: out of the final 1137 accepted sources in the Mateos et al. sample, only 119 would have been excluded by our criteria.

2.4. Sensitivity maps

The value of the sensitivity map at a given point is the minimum count rate for a source to be detected with the desired likelihood at that point. As explained above, the detection likelihood assigned by `emldetect` takes into account the number of counts in the detection box, how well they fit the PSF shape and the variation of the exposure map over the detection box. The likelihood is therefore, in principle, not trivially related to the Poisson probability of an excess in the number of detected counts over the expected background in the detection box.

However, we have found (see Appendix A) that the count rate assigned by the software to the source (the "observed" count rate) is proportional to the count rate expected from a Poisson distribution for the same likelihood (for detection likelihoods between 8 and 20), with proportionality constant ∼0.9−1.1 depending on the band. It appears that the non-Poisson characteristics taken into account by `emldetect` have a relatively small influence on the determination of the count rate. For a given likelihood, radius of the detection region, total value of the background map and average value of the exposure map in that region we calculated the expected Poisson count rate at each point of the detector using the proportionality constants for the corresponding "observed" count rate, i.e. the value of the sensitivity map (see Appendix A for further details).

We have used the above procedure to create sensitivity maps for each field in each band in image (X, Y) coordinates, which have 4 arcsec pixels with sky North towards the top and East to the left and are centred approximately in the optical axis of the X-ray telescope. We have also taken into account for each field the areas excluded close to the detector edges, and around the bright sources and OOT regions, excluding those regions from the sensitivity maps as well.

The final selection of sources in each band was done using their detection likelihood and the corresponding sensitivity map at their given sky position (to ensure the validity of the sky areas calculated from the sensitivity maps, see Sect. 4.1). We have chosen a detection confidence limit of 5-σ which corresponds to $L = 15$ in the band under consideration. We have also imposed that the source has a count rate equal to or larger than the value of the sensitivity map at that sky position, to ensure that the source detection is reliable. This excluded less than 5% of the $L \geq 15$ sources in the soft band, ∼10% of the sources in the XID and ultra-hard bands and ∼20% of the sources in the hard band. The number of sources excluded by this criterion is much larger in the hard band than in the other bands. This somewhat contradicts the proportionality between the detected count rate and the Poisson count rate for this band being in a different direction than in the other bands (∼10% smaller rather than ∼10% larger, see Table A.1), since the sensitivity map will then be relatively lower and therefore would tend to include more sources rather than exclude them. In any case, the hard band is the widest and the only one of our bands which is not one of the bands used for source searching in the SAS, being instead a composite of three default bands. In principle, all this makes the hard band the more complex to deal with and for which therefore the uncertainties associated with our empirical method to calculate the sensitivity maps might be highest.

The total number of distinct selected sources, that is fulfilling the above criteria in at least one of the bands, is 1433. We give in Table 4 the total number of selected sources in each of the above bands. Unless explicitly stated otherwise, for the $\log N - \log S$ and the angular clustering analyses below we have only used sources detected in the corresponding bands. However, it is important to emphasise that if a source has been detected in at least one band it can be considered to be a real source and therefore its counts in other bands can be used, e.g. for spectral fitting or hardness ratio calculations, even if the source has a count rate smaller than the detection threshold in those bands.

To estimate the number of spurious sources in our survey we first need to calculate the number of independent source detection cells. `emldetect` uses an input list from `eboxdetect`, which is a simple sliding-box algorithm using a square 5× 5 pixels detection cell. Therefore the individual detection cell is $5 \times 5 \times (4'')^2 = 400$ arcsec^2. The total area of our survey is ∼4.8 deg^2 (see Sect. 4.1) or about 155 520 independent detection cells. Since the probability of a false detection at the 5-σ level is 0.000057, this corresponds to about 9 spurious sources in each of our detection bands. This is less than 1% in the soft and XID bands, about 2% in the hard band and almost 10% in the ultra-hard band. The latter fraction could partly explain the discrepant point in the ultra-hard $\log N - \log S$ at the lowest fluxes (see Sect. 4.5), since it is there where the contribution from spurious sources is expected to be highest.

3. X-ray properties of the sources

We have studied the broad spectral characteristics of our sources by fitting their count rates in several bands to those expected from power-law spectra with photon index Γ and Galactic Hydrogen column densities ($N_{\rm H}$) from 21 cm radio measurements (Dickey & Lockman 1990, see Table 1). The spectra of a few sources will obviously not be well represented by a power-law (e.g. stars or clusters showing thermal spectra), but for the purpose of calculating fluxes in bands in which the power-law was fit, a power-law is a reasonably accurate and very simple approximation.

The expected count rates for different values of Γ (from −10 to 10 in steps of 0.5, interpolating linearly for intermediate values) and the Galactic $N_{\rm H}$ values of each field were calculated with `xspec` (Arnaud 1996), using the "canned" on-axis redistribution matrix files and on-axis effective areas for each field created with the SAS task `arfgen`. The inaccuracies arising from using standard response matrices instead of source specific matrices (as generated by `rmfgen`) are expected to be small since we only use broad bands, much broader than the spectral resolution of the EPIC pn camera. Since the count rates from `emldetect` are corrected for the exposure map (which includes vignetting and bad pixel corrections) and the PSF enclosed energy fraction, the effective areas were generated while disabling the vignetting and PSF corrections, as indicated in the `arfgen` documentation.

The corresponding fluxes in bands 2 to 5 (in the case of band 5 the flux was calculated in the 7.5 to 10 keV band) were also calculated using the spectral model for the same values of Γ, setting $N_{\rm H} = 0$. We have checked that the relatively coarse sampling does not introduce any biases in our spectral fits by repeating the spectral fits for one field with a step in Γ of 0.001. The results were essentially identical with any differences in the spectral slopes being much smaller than their uncertainties.

We have performed spectral fits in bands 2 and 3 (for the soft and XID fluxes) and bands 3, 4 and 5 (for the hard and ultra-hard fluxes). The average count rates of our selected sources in the XID and hard bands are 0.0095 and 0.0032, respectively, which for a typical exposure time of 15 ks give an average of more than 10 counts per bin. This ensures that Gaussian statistics are a good approximation here. However, these count rates are not sufficient in many cases to warrant a detailed spectral fitting with `xspec`. The best fit Γ and flux were calculated by minimising the χ^2 between the observed and expected count rates. The minimisation was actually done in Γ, setting the flux from the normalisation that minimised the χ^2 in the corresponding band. One sigma error bars for the photon index and flux were obtained from the values which produced $\Delta\chi^2 = 1$ from the minimum. These error bars were asymmetric in most cases but we have used a symmetric error bar (the arithmetic average of the upper and lower error bars) for the weighted averages of the spectral slopes and the $\log N - \log S$. In a few cases the fitted photon indices are very steep with $|\Gamma| \sim 10$. In all cases this corresponds to sources

Table 4. Number of sources selected in different bands N, weighted average slopes $\langle\Gamma\rangle$ and errors (taking into account both the error bars in the individual Γ and the dispersion around the mean), and number of observed sources used in the average $N_{\rm ave}$. The soft, hard, XID and ultra-hard bands are as defined in the text. "Soft and hard" refers to sources selected simultaneously in the soft and hard bands, "Only soft" refers to sources selected in the soft band but not in the hard band, and "Only hard" refers to sources selected in the hard band and not in the soft band.

		0.5–4.5 keV		2–10 keV	
Selection	N	$N_{\rm ave}$	$\langle\Gamma\rangle$	$N_{\rm ave}$	$\langle\Gamma\rangle$
Soft	1267	1239	1.811 ± 0.015	1145	1.53 ± 0.02
Hard	397	397	1.76 ± 0.03	394	1.55 ± 0.03
XID	1359	1335	1.773 ± 0.016	1244	1.47 ± 0.02
Ultra-hard	91	91	1.80 ± 0.06	91	1.50 ± 0.07
Soft and hard	345	345	1.79 ± 0.03	342	1.67 ± 0.03
Only soft	922	894	1.878 ± 0.017	803	1.04 ± 0.04
Only hard	52	52	-0.29 ± 0.08	52	0.53 ± 0.12

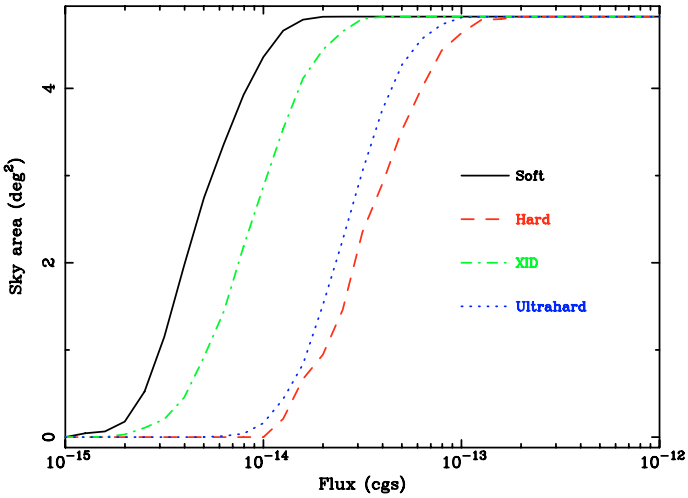

Fig. 1. Sky area as a function of flux for different bands.

with positive count rates in only one of the fitted bands, forcing the power law to the steepest allowed slope. The number of these pathological cases in each band can be obtained from the difference between the N and $N_{\rm ave}$ columns in Table 4 (typically <10%).

The photon indices and fluxes in each of the fitted bands as well as their error bars are given for each source in Table 3. We show in Table 4 the weighted average photon indices of the detected sources in each of the fitted bands as well as the number of sources used in the averages, excluding in all cases sources with $|\Gamma| > 9$ to avoid biasing the averages with a few outliers. The impact of excluding these sources would be small for the weighted averages used here.

We have checked the reliability of our simple spectral fit method (see Appendix B), performing both internal tests with simulations and external checks with respect to the full spectral fits of Mateos et al. (2005) to a set of sources with a large overlap. We conclude that our 2–3 band spectral slopes are sufficient when taken individually for the purposes of calculating fluxes in different bands. However, we have found that there are significant systematic biases in the average photon indices, when averaged over large samples, which are larger than the statistical errors. These systematic biases are nonetheless small in both absolute ($\Delta\Gamma \sim 0.12$) and relative ($\Delta\Gamma/\Gamma = 0.2$) terms. Our method is therefore adequate for extracting broad spectral information from medium flux X-ray sources such as those in the 1XMM and 2XMM catalogues.

In broad terms, the soft/XID band slopes are ~1.8 for sources detected in all bands, being slightly softer for sources detected only in the soft band and much harder for sources detected only in the hard band (see Table 4). The hard band slopes are flatter, closer to 1.5–1.6, but slightly steeper for sources detected both in the soft and hard bands (~1.7). The average hard slope of the sources only detected in the soft band is quite flat $\langle\Gamma\rangle \sim 1$, but their un-weighted average is $\langle\Gamma\rangle = 1.53 \pm 0.08$, much closer to the other average slopes in that band. The origin of this difference is that "Only soft" sources with steep spectra in the hard band tend to have larger errors in the hard spectral slope (because they have few counts in *XMM-Newton* bands 4 and 5 and so the slope is not well constrained), and therefore they have a very small weight in the weighted average.

The difference between the spectral slopes of sources only detected in in the soft band and those only detected in the hard band is partly due to a known bias in likelihood limited surveys such as this that occurs because source detection is done in photons rather than in flux (Zamorani et al. 1988; Della Ceca et al. 1999), so that for a given flux softer sources will be much easier to detect in the soft band while the inverse would be true for harder sources. This is compounded by the fact that *XMM-Newton* is much more sensitive to soft photons.

4. log N–log S

We firstly studied the sky density of the detected sources as a function of flux (known as $\log N - \log S$) in the soft, hard, XID and ultra-hard bands.

4.1. Sky areas

The sky area over which we are sensitive to a given flux is easy to calculate from the sensitivity maps. In principle, it is just necessary to sum the sky area for which the sensitivity maps have values below the desired flux. However, the conversion between flux and count rate depends on the assumed spectral shape. In each band i, we have calculated the sky areas at each flux for each assumed spectral slope $\Omega_i(S, \Gamma)$ with the following procedure: in each field we have converted S to count rate using Γ and the response matrices and summed the area for which the sensitivity map is below that count rate. The total sky area is the sum of the areas found for each field.

The sky area in each band for each source j is then $\Omega_{j,i} = \Omega_i(S_{j,i}, \Gamma_{j,i})$, where the source's flux $S_{j,i}$ and spectral slope $\Gamma_{j,i}$ are described in Sect. 3.

Sky areas independent of any assumed spectrum can also be obtained by weighting $\Omega_i(S, \Gamma)$ with the number of detected sources in each (S, Γ) bin. We will call these spectrally averaged sky areas $\Omega_i(S)$. They are shown in Fig. 1. The maximum value of all curves is 4.8 deg^2, which is the geometric area covered by our survey, taking into account the excluded areas.

We have also obtained spectrally averaged sky areas for each field $\Omega_{i,k}(S)$ ($k = 1 \ldots$ number of fields) from the sensitivity maps for each field k in each band i, using $S(\Gamma)$ for that field and weighting with the number of sources in the total sample with the corresponding S, Γ, assuming implicitly that all fields have the same $S(\Gamma)$ distribution.

4.2. Data from other surveys

Our survey consists of *XMM-Newton* exposures with a typical exposure time of about 15 ks and it is hence a medium survey. Shallower, wider area surveys are required to obtain significant numbers of bright sources while deeper pencil-beam surveys will probe fainter fluxes. We have combined our survey with both shallower and deeper surveys to obtain a wide coverage in flux (∼2–4 orders of magnitude):

- BSS: Della Ceca et al. (2004) have constructed a bright sample of *XMM-Newton* sources down to a flux of 7×10^{-14} cgs in the XID band, with a uniform coverage of 28.1 deg^2 above that flux. This sample ideally complements our survey, being both wider and shallower and selected exactly in the same band with the same telescope (but with a different detector: MOS2 instead of pn). We have used a total of 389 sources from that survey, including all sources identified as stars which have been excluded from the $\log N - \log S$ analysis of Della Ceca et al. (2004)
- HBS: in the same paper, Della Ceca et al. (2004) also define a sample of sources detected in the ultra-hard band, down to the same flux limit and with a uniform coverage of 25.17 deg^2, again both shallower and wider than ours and with the same telescope. Results from a subsample are presented by Caccianiga et al. (2004). The source counts are also discussed by Della Ceca et al. (2004) and compared to previous results from *BeppoSAX*. We have used a total of 65 sources from this survey
- CDF: the deepest survey in the soft and hard bands so far is the *Chandra* Deep Field North (CDF-N), Bauer et al. (2004), obtained from a total exposure of 2 Ms in a Northern hemisphere location. In a complementary effort in the South, the *Chandra* Deep Field South (Giacconi et al. 2001; Rosati et al. 2002) obtained a total exposure time of 1 Ms. Source counts from both samples have been discussed in Bauer et al. (2004). There are a total of 442 soft and 313 hard sources in the CDF-N, and 282 soft and 186 hard sources in the CDF-S. Recent internal *Chandra* calibrations have increased the estimate of the ACIS effective area above 2 keV. We have used procedures available in the *Chandra* calibration database to compare data from Cycles 8 and 5: above 2 keV the ratio between the effective areas is reasonably flat and well approximated by a constant increase factor of about 12%. The increase in the 2–8 keV fluxes is unlikely to be due to the increasing contamination from the optical blocking filter, since the latter only manifests itself below 1 keV. Therefore, all CDF-N and CDF-S hard fluxes (and their corresponding errors) have been decreased by this factor. Furthermore, when comparing the sky areas calculated individually for each source with those calculated interpolating from the sky area of the full survey, the faintest soft sources in both CDF surveys showed large (up to several orders of magnitude) discrepancies. Since our maximum likelihood $\log N - \log S$ fit method requires the use of a model for the sky area of the full survey (see Sect. 4.5), we have not used soft sources fainter than 3 and 7×10^{-17} cgs in the CDF-N and CDF-S respectively for fits to $\log N - \log S$.
- AMSS: The *ASCA Medium Sensitivity Survey* (Ueda et al. 2005) is one of the largest high Galactic latitude, broad-band X-ray surveys to date and includes 606 sources over 278 deg^2 with hard band fluxes between $\sim 10^{-13}$ and $\sim 10^{-11}$ cgs.

The average sky area as a function of flux for different bands for the CDF and AMSS are shown in Bauer et al. (2004) and Ueda et al. (2005), respectively, and we have used these values (as supplied by the authors) for the Maximum Likelihood fit (see Sect. 4.5). The *Chandra* re-calibration has also been applied to the CDF effective area fluxes.

4.3. Construction of the binned log N – log S

The binned differential $\log N - \log S$ (number of sources per unit flux and unit sky area at a given flux S: $\mathrm{d}N/\mathrm{d}S\,\mathrm{d}\Omega$) have been constructed by summing the inverse of the $\Omega_{j,i}$ for the sources in each flux bin and dividing that number by the width of the bin. The errors are calculated by dividing the $\mathrm{d}N/\mathrm{d}S\,\mathrm{d}\Omega$ by the square root of the sources in each bin. Since we have chosen to have a minimum number of sources per bin (see below), their widths are all in principle different and are determined by the flux of the first source in the bin and the flux of the first source in the next bin as flux increases. By this definition, the width of the last bin is left undefined. Since we have a large number of sources we have dropped the brightest source in each sample (only when dealing with binned $\log N - \log S$) and defined the upper limit in the last bin to be the flux of this brightest source.

The integral $\log N - \log S$ relation (number of sources per unit sky area with fluxes higher than S: $N(>S)$) from our sample and other samples are shown in Fig. 2. We have chosen to plot the integral $\log N - \log S$ relation in bins containing 15 sources each (except the last one, which can contain up to 29 sources), to avoid apparent features due to fluctuations of a few sources, especially at the brighter ends of each sample where the number of sources is low. We have simply added the inverse of the sky areas for each source, $\Omega_{j,i}$, for all sources with fluxes above the lower limit of each bin. The error bars are calculated by dividing the $N(>S)$ by the square root of the total number of sources with flux equal or greater than the lower limit of the bin.

Sources just below the faint flux limit of a survey may be subject to statistical fluctuations in their fluxes that promote them into the survey. Similarly, the fainter sources just above that limit could drop out of the survey for the same reason. However, since fainter sources are much more abundant (because the source counts are steep), the net effect is to artificially increase the observed source counts close to the fainter survey limits. This is known as the Eddington bias (Eddington 1913) and may lead to a re-steepening of $\log N - \log S$ at the faintest fluxes, as observed in the AXIS ultra-hard source counts for example.

4.4. log N – log S model

Previous X-ray source count results (e.g. Bauer et al. 2004; Ueda et al. 2003; Moretti et al. 2003; Baldi et al. 2002; Hasinger et al. 1998; Cagnoni et al. 1998) have shown that $\log N - \log S$ is well approximated by a steep power law at bright fluxes and flattening at lower fluxes. We have hence adopted the following model for the differential $\log N - \log S$:

$$\frac{\mathrm{d}N}{\mathrm{d}S\,\mathrm{d}\Omega}(S) = \left\{ \begin{array}{ll} \frac{K}{S_\mathrm{b}} \left(\frac{S}{S_\mathrm{b}}\right)^{-\Gamma_\mathrm{d}} & , S \leq S_\mathrm{b} \\ \frac{K}{S_\mathrm{b}} \left(\frac{S}{S_\mathrm{b}}\right)^{-\Gamma_\mathrm{u}} & , S > S_\mathrm{b} \end{array} \right\}.$$

The above model has four independent parameters: the break flux S_b, the normalisation K, the slope at high fluxes Γ_u and the slope at low fluxes Γ_d. If the change in the slope of $\log N - \log S$ is not significant we fixed $S_\mathrm{b} \equiv 10^{-14}$ cgs and $\Gamma_\mathrm{u} = \Gamma_\mathrm{d}$, leaving only two independent variables: K and Γ_u.

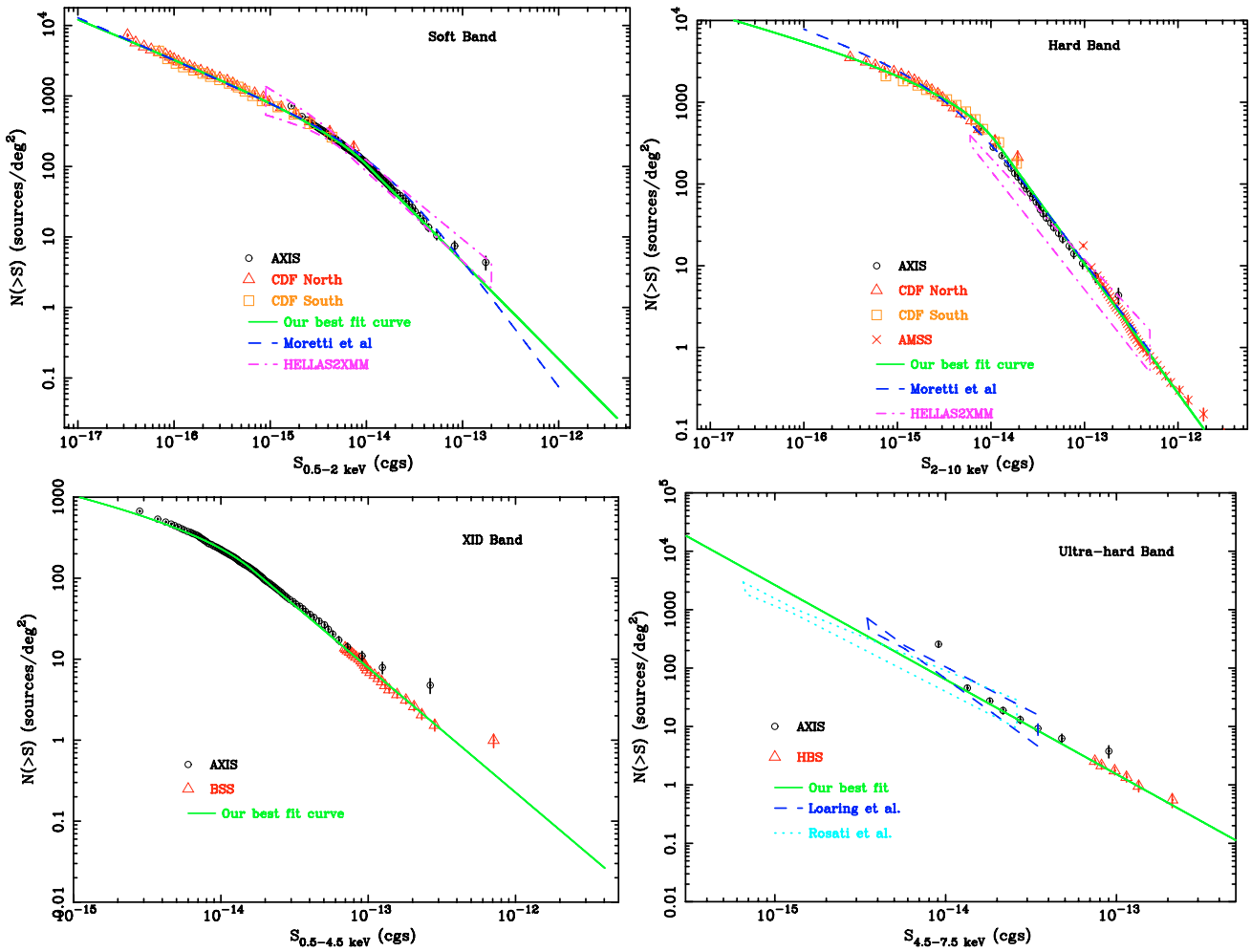

Fig. 2. Integral $\log N - \log S$ in different bands, along with our best fits and some previous results

The integral $\log N - \log S$ relation is therefore:

$$N(>S) = \int_S^\infty \mathrm{d}S \frac{\mathrm{d}N}{\mathrm{d}S\,\mathrm{d}\Omega}(S).$$

Finally, assuming a given $\log N - \log S$, the number of sources with fluxes between $S_{\min}$ and $S_{\max}$ is

$$N(S_{\min} \le S \le S_{\max}) = \int_{S_{\min}}^{S_{\max}} \mathrm{d}S \frac{\mathrm{d}N}{\mathrm{d}S\,\mathrm{d}\Omega}(S)\Omega(S).$$

This number is the total expected number of sources in our survey λ with fluxes in band i in that interval if $\Omega(S) = \Omega_i(S)$ defined above, or it can be λ_k: the expected number of sources in that flux interval and band in a given field k where $\Omega(S) = \Omega_{i,k}(S)$.

The contribution to the intensity of the XRB from the interval $(S_{\min}, S_{\max})$ is

$$I(S_{\min} \le S \le S_{\max}) = \int_{S_{\min}}^{S_{\max}} \mathrm{d}S\, S \frac{\mathrm{d}N}{\mathrm{d}S\,\mathrm{d}\Omega}(S). \quad (1)$$

4.5. Maximum likelihood fit method and results

We have fitted $\log N - \log S$ using a Maximum Likelihood method which takes into account the uncertainties in the fluxes of the sources, as well as the changing shape of the sky areas with flux.

Specifically, we have minimised the following expression:

$$L_{\mathrm{tot}} = \sum_{\mathrm{sample}} L_{\mathrm{sample}},$$

where L_{sample} is given by

$$L_{\mathrm{sample}} = -2 \sum_{j=1}^{N} \log(P(S_j)) - 2\log(P_\lambda(N)) \quad (2)$$

and where the sum is over all N sources in the corresponding sample. $P(S_j)$ is the probability of finding a source of flux S_j in that sample (see below). The second term is $P_\lambda(N) = \mathrm{e}^{-\lambda}\lambda^N/N!$, the Poissonian probability of finding N sources in that sample when the expected number is λ (see Sect. 4.4).

We have defined $P(S_j)$ as

$$P(S_j) = \frac{\int_{S'_{\min}}^{S'_{\max}} \mathrm{d}S \frac{\mathrm{d}N}{\mathrm{d}S\,\mathrm{d}\Omega}(S)\Omega(S) \frac{\exp\left(\frac{-(S_j-S)^2}{2\sigma_j^2}\right)}{\sqrt{2\pi}\sigma_j}}{\lambda}.$$

This expression takes into account both the variation of the sky area with flux, through $\Omega(S)$, and the uncertainty in the flux of the source σ_j (Page et al. 2000) through the last exponential term in the numerator, in which we have assumed a Gaussian distribution of the fluxes around the measured value.

Table 5. Maximum likelihood fit results to $\log N - \log S$ in different bands and using different samples: the first column is the band used, the second is the power-law slope above the flux break, the third is the slope below that break, the fourth is the flux break, the fifth is the normalisation and the last six columns indicate the number of sources from each sample used in the fit.

Band	Γ_u	Γ_d	S_b (10^{-14} cgs)	K (deg^{-2})	N_{used}/N_{tot} AXIS	BSS	HBS	CDF-N	CDF-S	AMSS
soft[g]	$2.40^{+0.06}_{-0.07}$	$1.74^{+0.06}_{-0.07}$	$1.15^{+0.18}_{-0.19}$	120.0^{+22}_{-18}	1267/1267					
soft	$2.39^{+0.06}_{-0.06}$	$1.69^{+0.07}_{-0.06}$	$1.15^{+0.16}_{-0.13}$	$123.4^{+18.8}_{-17.1}$	1267/1267					
soft[f]	$2.38^{+0.14}_{-0.09}$	$1.56^{+0.01}_{-0.01}$	$1.02^{+0.14}_{-0.17}$	$141.4^{+42.1}_{-7.3}$	1267/1267			429/442[a]	269/282[b]	
hard[g]	$2.74^{+0.08}_{-0.07}$	-	1.00	735^{+92}_{-76}	348/397[c]					
hard	$2.72^{+0.07}_{-0.08}$	-	1.00	$684.4^{+74.1}_{-84.0}$	348/397[c]					
hard	$2.03^{+0.12}_{-0.11}$	$1.00^{+0.11}_{-0.12}$	$0.30^{+0.07}_{-0.05}$	$1086.6^{+134.3}_{-146.5}$				313/313		
hard	$2.51^{+0.50}_{-0.28}$	$0.89^{+0.12}_{-0.12}$	$0.72^{+0.11}_{-0.10}$	$743.7^{+109.6}_{-105.6}$					186/186	
hard	$2.12^{+0.13}_{-0.01}$	$1.10^{+0.01}_{-0.01}$	$0.44^{+0.04}_{-0.01}$	$799.1^{+226.8}_{-8.4}$				313/313	186/186	
hard	$2.66^{+0.08}_{-0.05}$	$1.20^{+0.01}_{-0.01}$	$1.00^{+0.08}_{-0.01}$	$611.5^{+49.1}_{-34.3}$	397/397			313/313	186/186	
hard	$2.58^{+0.02}_{-0.02}$	-	1.00	$606.5^{+46.8}_{-46.3}$	348/397[c]					606/606
hard	$2.53^{+0.25}_{-0.18}$	$1.18^{+0.14}_{-0.08}$	$0.92^{+0.66}_{-0.19}$	$607.8^{+366.4}_{-208.1}$				313/313	186/186	606/606
hard[f]	$2.58^{+0.17}_{-0.02}$	$1.30^{+0.01}_{-0.01}$	$1.17^{+0.01}_{-0.05}$	$485.3^{+10.1}_{-24.3}$	397/397			313/313	186/186	606/606
XID[g]	$2.39^{+0.05}_{-0.20}$	$1.37^{+0.09}_{-0.32}$	$1.08^{+0.07}_{-0.48}$	265^{+214}_{-19}	1359/1359					
XID	$2.46^{+0.11}_{-0.07}$	$1.29^{+0.09}_{-0.18}$	$1.45^{+0.16}_{-0.26}$	$212.2^{+47.4}_{-22.8}$	1359/1359					
XID[f]	$2.54^{+0.03}_{-0.04}$	$1.35^{+0.06}_{-0.25}$	$1.64^{+0.13}_{-0.28}$	$193.0^{+33.1}_{-15.8}$	1359/1359	389/389				
ultra-hard[g]	$2.63^{+0.15}_{-0.15}$	-	1.00	102^{+23}_{-20}	84/89[d]					
ultra-hard	$2.59^{+0.09}_{-0.05}$	-	1.00	$95.0^{+11.1}_{-12.8}$	84/89[d]					
ultra-hard[f]	$2.62^{+0.10}_{-0.10}$	-	1.00	$102.2^{+20.0}_{-21.1}$	84/89[d]		58/65[e]			

[a] $S_{min,CDF-N} = 3 \times 10^{-17}$ cgs; [b] $S_{min,CDF-S} = 6 \times 10^{-17}$ cgs; [c] $S_{min,AXIS} = 1.5 \times 10^{-14}$ cgs; [d] $S_{min,AXIS} = 10^{-14}$ cgs; [e] $S_{max,HBS} = 2.5 \times 10^{-13}$ cgs; [f] Best fit used for contribution to XRB, and in Figs. 2 and 3; [g] Using fixed photon indices of 1.8 in the soft and XID bands, and 1.7 in the hard and ultra-hard bands.

To speed up the numerical calculation of the integral in the numerator above we have defined $S'_{min} = \max(S_j - 4\sigma_j, S_{min})$ and $S'_{max} = \min(S_j + 4\sigma_j, S_{max})$, since the tails of the Gaussian distribution decrease very quickly. The normalisation of $\log N - \log S$ (K) appears both in the numerator and the denominator of $P(S_j)$ and it is unconstrained. This is why we have introduced the second term in Eq. (2).

The 1-σ uncertainties in the $\log N - \log S$ parameters are estimated from the range of each parameter around the minimum which makes $\Delta L_{tot} = 1$. For each parameter this is performed by fixing the parameter of interest to a value close to the best fit value and varying the rest of the parameters until a new minimum for the likelihood is found. This procedure is repeated for several values of the parameter until this new minimum equals $L_{tot,min} + 1$.

The results of the Maximum Likelihood fits to various (single and combined) samples and bands are given in Table 5. Except when stated otherwise the flux interval used in the fit is $S_{min} = 10^{-17}$ cgs and $S_{max} = 10^{-12}$ cgs. These numbers have been chosen to span the observed fluxes of the sources. The final results are not very dependent on them, since the sky area falls very quickly at low fluxes and the sky density of bright sources is very small. The initial values for the numerical search for the best fit have been obtained from a χ^2 fit to the total binned differential $\log N - \log S$. The best overall fits are marked in the first column of Table 5 and also shown in Fig. 2.

The first two rows in Table 5 for each band allow comparison of the results of the fit to the AXIS sources, using a fixed spectral slope to calculate fluxes and sky areas ($\Gamma = 1.8$ in the soft and XID bands, $\Gamma = 1.7$ in the hard and ultra-hard bands, first row), to the results using the best fit spectral slope for each source (second row). The results are mutually compatible in all bands but the error bars are noticeably larger in the XID and ultra-hard band when using a fixed spectral slope. In fitting the spectra of the sources we effectively "force" them to have a power law spectral shape and hence the uncertainties in the fitted fluxes are smaller than those in the fluxes with fixed spectral slopes. This might at least partly explain the smaller uncertainties in the $\log N - \log S$ fitted parameters in the latter case. In what follows we have thus used the slopes from spectral fits to calculate fluxes from count rates for all the AXIS sources, since this approach seems to produce smaller uncertainties in the fitted parameters.

There is general agreement between data and model fits but it is difficult to quantify this statement, since, unlike the χ^2 statistic, the absolute value of L_{tot} is not an indicator of the goodness of fit. Each panel in Fig. 2 covers several orders of magnitude and hence a detailed visual comparison is also difficult. We have therefore plotted in Fig. 3 the ratio between the binned differential $\log N - \log S$ and the best fit model. Systematic deviations from unity in those plots would reveal differences between the data and the best fit model. In that Figure we also show the 1-σ uncertainty interval on the best fit which is estimated in a conservative manner: for each flux we have calculated the differential $\log N - \log S$ in the 16 corners of the hypercube defined by the 1-σ uncertainty intervals in the best fit $\log N - \log S$ parameters and taken the maximum and minimum values.

As expected, the relative agreement of the AXIS and BSS/HBS source counts is quite good, merging with each other well and following the same $\log N - \log S$ shape. This confirms the good relative calibration of the two EPIC cameras on board *XMM-Newton* (pn for AXIS and MOS2 for BSS/HBS). The XMM-COSMOS $\log N - \log S$ results (Cappelluti et al. 2007) are also consistent with our results within 1 to 2-σ in the soft and hard bands, but the uncertainties in our best fit parameters

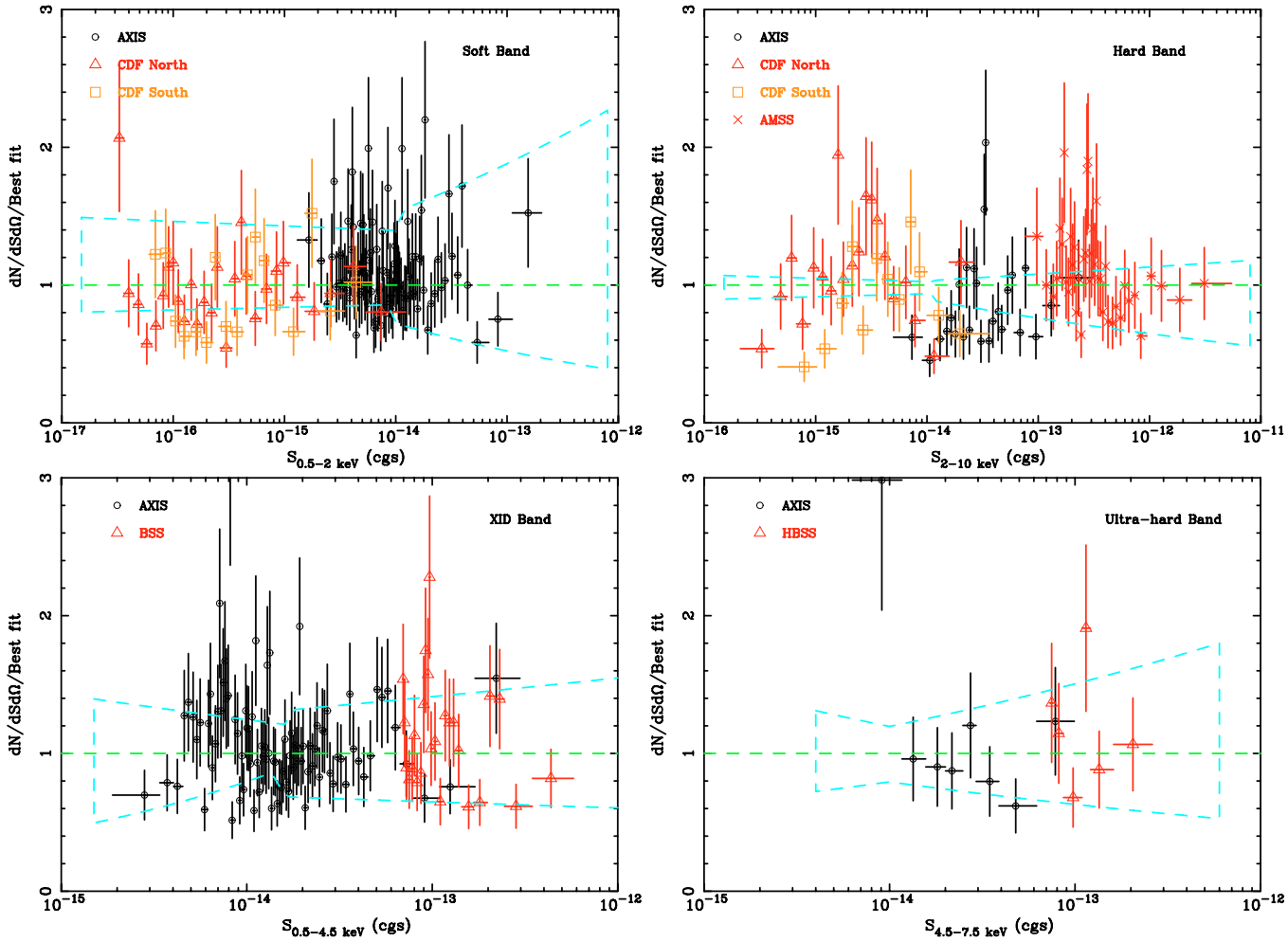

Fig. 3. Ratio between the binned differential $\log N - \log S$ and the best fit model in different bands. The 1-σ uncertainty interval in $\log N - \log S$ is also shown as bow-tie-shaped dashed lines above and below unity.

are smaller, probably due to our much higher number of sources and wider flux coverage in those bands.

The agreement with the CDF samples is very good. In the soft band our joint AXIS-CDF fit is in excellent agreement with the CDF results of Bauer et al. (2004) ($\Gamma_{\rm d} = 1.55 \pm 0.03$), as expected since virtually all sources at low fluxes are the same in both samples. Our AXIS-only fit prefers a steeper slope below the break, but still compatible with the joint AXIS-CDF fit at $<2\sigma$. The agreement with Moretti et al. (2003) is very good below the break ($\Gamma_{\rm d} = 1.60^{+0.02}_{-0.03}$ and hereafter we have translated all integral $\log N - \log S$ slopes to our differential slopes), but their break happens at higher fluxes ($S_{\rm b} = (1.5 \pm 0.3) \times 10^{-14}$ cgs), resulting in a steeper slope at high fluxes ($\Gamma_{\rm u} = 2.82^{+0.07}_{-0.09}$). Our results are fully compatible with those of the HELLAS2XMM (Baldi et al. 2002) sample at their low flux end, but our source counts are systematically at their lower envelope values above the break.

In the hard band the CDF, AXIS and AMSS $\log N - \log S$ results match well in their overlapping regions. However, the ratio in the top-right panel of Fig. 3 is rather uncertain and shows clear differences in detail. The AXIS data lie mostly below the model predictions, perhaps because of the high fraction of sources excluded for being fainter than the sensitivity map (see Sect. 2.4) and also the relatively lower values of the sensitivity map with respect to the Poissonian count rate (which would in turn increase the effective area). There are two "bumps", with the data systematically above the model at about 3×10^{-15} and 3×10^{-13} cgs (although in this last case the discrepancy is well inside the uncertainties of the $\log N - \log S$ fit). These bumps probably arise from fitting a broken power-law, with a sharp break to the $\log N - \log S$, which is really a smooth distribution coming from the superposition of different populations at different redshifts. This is compounded by possible calibration uncertainties: the hard band calibration of *Chandra* has changed by 12% in the last 3 years (see Sect. 4.2).

A break at 3×10^{-15} cgs is actually present in the joint fit to the CDF-N and CDF-S hard (all-CDF) samples (see Table 5), with the low flux slope compatible with the value from Bauer et al. 2004 ($\Gamma_{\rm d} = 1.56 \pm 0.14$) within about 1-$\sigma$ and the high flux slope flatter than in the global fit. The low flux slopes for the two single CDF samples are much flatter and incompatible with any previously reported values ($\sim$1). We believe that the change in the slope of the source counts between AXIS and the CDF forces the global break flux to the overlapping fluxes between those samples ($\sim 10^{-14}$ cgs). Hence the fit below this flux somehow averages the two slopes present in the CDF, forming a bump around the CDF break, rising and dropping above and below this flux respectively. The overall behaviour of the $\log N - \log S$ can be obtained by a fit to the CDF and AMSS data alone and, despite the lower AXIS source counts, the best fit values between the CDF+AMSS and the CDF+AMSS+AXIS are mutually compatible within $<$1-σ. The main effect is to push

the break flux to higher fluxes and steepen the low flux slope. Additionally, the uncertainties in all parameters are significantly reduced by the inclusion of the AXIS data, by factors between about 2 and 20.

The best fit curve by Moretti et al. (2003) is again very similar to our all-sample fit at the highest ($\Gamma_u = 2.57^{+0.10}_{-0.08}$) and lowest fluxes ($\Gamma_d = 1.44^{+0.12}_{-0.13}$), where however it is above the CDF data (perhaps because of the change in the hard band calibration of *Chandra*). Their transition flux occurs at lower fluxes ($S_b = (4.5^{+3.7}_{-1.7}) \times 10^{-15}$ cgs), compatible with the CDF-N and all-CDF fits, perhaps because their functional form is smoother than a broken power-law and cannot accommodate the relatively strong break between the AMSS/AXIS steep slope and the CDF. The HELLAS2XMM confidence interval overlaps with ours but has a flatter slope and falls clearly below both the AXIS and the CDF points below about 2×10^{-14} cgs, perhaps suggesting incompleteness at their lower fluxes.

Our fit to the joint AXIS-BSS source counts in the XID band looks visually quite good, passing through the middle of the AXIS and BSS data points (see Fig. 2). The XID band source counts from the BSS (Della Ceca et al. 2004) require a steeper slope ($\Gamma_u = 2.80 \pm 0.11$) than both our AXIS-only and AXIS+BSS fits. The origin of this apparent discrepancy is probably that we have used all the selected sources in both samples, while they have excluded the stars, which contribute more at higher fluxes and hence would produce a steeper source count distribution, as observed.

The AXIS-only ultra-hard source counts merge smoothly with the HBS if we ignore our higher flux point (which could be affected by the exclusion of the bright targets in our survey). We have not used AXIS sources with fluxes below 10^{-14} cgs in the fit because the $\log N - \log S$ steepens suddenly at those fluxes, perhaps because the Eddington bias is most important in this band where the number of sources is smallest, and/or because of the contribution from spurious sources. The best fit values, including these lowest flux sources, are very similar to the ones excluding them but the errors on the values are much larger. Since the ML fit is dominated by the bulk of the sources, rather than by a few discrepant points, and given the low number of sources the AXIS-only and AXIS+HBS source counts are very similar and mutually compatible. They are also compatible as well with the HBS-only value ($\Gamma_u = 2.64^{+0.25}_{-0.23}$), despite the fact that this $\log N - \log S$ again only includes the extragalactic sources. The reason why the discrepancy is almost unnoticeable in the ultra-hard band is probably because the stars contribute negligibly to the high Galactic latitude source counts in this energy band.

We have compared our ultra-hard (4.5–7.5 keV) source counts to some previous results in the 5–10 keV band assuming a photon index of 1.7 for the flux conversion between these bands. Our source count slope is slightly steeper than in Baldi et al. (2002, $\Gamma_u = 2.54^{+0.25}_{-0.19}$) and flatter than in Loaring et al. (2005, $\Gamma_u = 2.80^{+0.67}_{-0.55}$), but well within the 1-σ limits in both cases. The source counts from Rosati et al. (2002, $\Gamma_u = 2.35 \pm 0.15$) are much flatter but still compatible with ours within less than 2-σ. They also find an indication of a break in the source counts at a 5-10 keV flux of 4×10^{-15} cgs (or about 3×10^{-15} cgs in the ultra-hard band). Since they also reach fainter fluxes ($S_{\rm ultra-hard} \sim 1.6 \times 10^{-15}$ cgs) their flatter source count slope probably arises from a combination of a Euclidean slope at brighter fluxes and an even flatter slope at their faintest fluxes. Our absolute source counts agree well with both Loaring et al. (2005) and Rosati et al. (2002) at their brightest flux limits and this agreement is maintained for our best fit $\log N - \log S$ over the whole flux interval in the former case, while the latter is clearly flatter and below our best fit, indicating a flattening of the ultra-hard source counts below our flux limit as discussed above. The XMM-COSMOS ultra-hard number counts coincide with ours at the lowest fluxes ($\sim 10^{-14}$ cgs) but they are above ours at higher fluxes, although within their relatively large error bars.

5. Contribution to the X-ray background

Using the best fit parameters from Table 5 we can estimate the intensity contributed by sources in different flux intervals (Eq. (1)). In order to compare the total intensity contributed by resolved sources with the total XRB intensity we need to estimate the intensity from sources brighter than our survey limit (see Sect. 5.1) and to adopt a total XRB intensity (see Sect. 5.2).

5.1. Intensity from bright sources and stars

The contribution from bright sources is straightforward to obtain for the "traditional" soft and hard bands. For the soft band we have followed the same method as Moretti et al. (2003), summing the fluxes of the sources in the *Rosat Bright Survey* (RBS, Schwope et al. 2000) with soft flux higher than 10^{-11} cgs, and dividing by the area covered by the RBS. For the hard band we have used the sources in the *HEAO-1* A2 survey (Piccinotti et al. 1982), which is complete down to 3.1×10^{-11} cgs. We have estimated the contribution of bright sources for the ultra-hard band from the hard band values, by converting both the flux limit and the intensity to the ultra-hard band using a power-law with slope $\Gamma = 1.7$. The XID band straddles the hard and soft bands and it is necessary to combine measurements taken in different bands and with different instruments. We have estimated the 2–4.5 keV flux limit and intensity from the hard band values using $\Gamma = 1.7$ again and then added both of them to the soft band values.

Since the estimates of the XRB intensity discussed below are for the extragalactic XRB we need to estimate the contribution from Galactic stars down to our fainter flux limits, in order to subtract it from our estimated source intensities and get the resolved fraction of the extragalactic XRB. We take the estimates of Bauer et al. (2004) from the fractions in their Table 2 and their assumed total XRB intensities: $0.19^{+0.05}_{-0.04} \times 10^{-12}$ and $0.36^{+0.34}_{-0.19} \times 10^{-12}$ cgs deg^{-2}, from stars in the soft and hard bands respectively. Since most of the contribution from stars comes from high fluxes (Bauer et al. 2004) and the stars at those fluxes have mainly low temperature thermal spectra (Della Ceca et al. 2004), we have estimated the stellar contribution in the XID band from the soft band contribution assuming a 0.5 MK `mekal` model under `xspec`, obtaining an XID-to-soft flux ratio of 1. Our estimate of the XID band intensity from Galactic stars is thus $0.19^{+0.05}_{-0.04} \times 10^{-12}$ cgs deg^{-2}. This is a conservative estimate, since the source counts in the XID band are about one order of magnitude shallower than in the soft band. Using that same spectral model, the stellar contribution in the 1–2 keV band is $(0.036 \pm 0.010) \times 10^{-12}$ cgs deg^{-2}. Given the even higher flux limit in the ultra-hard band and the strong dependence of the thermal spectrum with energy, we have instead estimated the stellar contribution to the ultra-hard band intensity by summing the fluxes of the two sources identified as stars in the HBS and dividing by the sky coverage of that survey, obtaining $(0.099 \pm 0.005) \times 10^{-12}$ cgs deg^{-2}. No sources have been identified as stars among the 60 sources identified in the XMS deeper ultra-hard survey (Barcons et al. 2007) and all of the 10 remaining unidentified objects in that sample are extended. This lower

Table 6. Intensity in different bands from different origins and flux intervals. The first column indicates the band, the second gives the origin of the intensity, the third and fourth columns list the flux interval, the fifth column the total intensity from that interval and the sixth column shows the fraction of the XRB intensity contributed by sources in that interval.

Band	Origin	$S_{\rm min}$ (cgs)	$S_{\rm max}$ (cgs)	$I(S_{\rm min} \le S \le S_{\rm max})$ (10^{-12} cgs deg^{-2})	$f_{\rm XRB}$
soft	Best fit AXIS+CDF $\log N - \log S$	0	3×10^{-17}	0.25	0.03
soft	Best fit AXIS+CDF $\log N - \log S$	3×10^{-17}	2×10^{-13}	5.60	0.75
soft	Best fit AXIS+CDF $\log N - \log S$	3×10^{-17}	10^{-11}	6.54	0.87
soft	RBS sources[a]	10^{-11}		0.20	0.03
soft	Total resolved	3×10^{-17}		6.55[e]	0.87
soft	XRB[b]			7.5 ± 0.4	
hard	Best fit AXIS+CDF+AMSS $\log N - \log S$	0	3×10^{-16}	0.62	0.03
hard	Best fit AXIS+CDF+AMSS $\log N - \log S$	3×10^{-16}	1×10^{-11}	17.08	0.85
hard	Best fit AXIS+CDF+AMSS $\log N - \log S$	3×10^{-16}	3.1×10^{-11}	17.18	0.85
hard	HEAO-1 A2 sources[c]	3.1×10^{-11}		0.43	0.02
hard	Total resolved	3×10^{-16}		17.25[e]	0.85
hard	XRB[b]			20.2 ± 1.1	
XID	Best fit AXIS+BSS $\log N - \log S$	3×10^{-15}	10^{-12}	8.48	0.56
XID	Best fit AXIS+BSS $\log N - \log S$	3×10^{-15}	2.38×10^{-11}	9.00	0.59
XID	Bright sources[d]	2.38×10^{-11}		0.39	0.02
XID	Total resolved	3×10^{-15}		9.20[e]	0.60
XID	XRB[d]			15.3 ± 0.6	
ultra-hard	Best fit AXIS+HBS $\log N - \log S$	9×10^{-15}	2×10^{-13}	1.50	0.21
ultra-hard	Best fit AXIS+HBS $\log N - \log S$	9×10^{-15}	1.05×10^{-11}	1.74	0.24
ultra-hard	Bright sources[d]	1.05×10^{-11}		0.15	0.02
ultra-hard	Total resolved	9×10^{-15}		1.79[e]	0.25
ultra-hard	XRB[d]			7.2 ± 0.4	

[a] Schwope et al. (2000). [b] Moretti et al. (2003). [c] Piccinotti et al. (1982). [d] See text. [e] After subtracting the stellar contribution (see Sect. 5.1).

fraction of stellar identifications of X-ray sources as the flux decreases and the band hardens is consistent with the average soft thermal X-ray spectra of stars and their flat source counts (Bauer et al. 2004).

5.2. Total X-ray background intensity

The total extragalactic XRB intensity measured with different instruments produces different results (Barcons et al. 2000) and not all the differences are attributable to cosmic variance. Moretti et al. (2003) have averaged several measurements available in the literature in the 1–2 keV and hard bands, obtaining 4.54 ± 0.21 and 20.2 ± 1.1 (in units of 10^{-12} cgs deg^{-2}), respectively. We have used those values to estimate the XRB intensity in our bands assuming a power-law with $\Gamma = 1.4$, which is an adequate model for the extragalactic XRB spectrum above 2 keV (Lumb et al. 2002). The extrapolation of the value of Moretti et al. (2003) in the hard band to the 1–2 keV band using that spectral shape produces a value similar to the one obtained directly by them in that band. This justifies extrapolating the same spectral shape again down to 0.5 keV, although the shape of the XRB is poorly known below 1 keV. The results are given in Table 6.

Our adopted hard band XRB intensity (from Moretti et al.) is in agreement with the estimate from Lumb et al. (2002, 21.5 ± 2.6 in the above units) and compatible with the result of De Luca & Molendi (2004, 22.4 ± 1.6) within about 1-σ. Extrapolating those intensities to the soft band using $\Gamma = 1.4$ we obtain 7.46 ± 0.09 and 7.78 ± 0.06, respectively, again fully compatible with our adopted value of 7.5 ± 0.4.

Recently, Hickox & Markevitch (2006, henceforth HM06) have re-estimated the total XRB intensity in the 1–2 keV and 2–8 keV bands, using *Chandra* CDF data and contributions from brighter sources. They have analysed thoroughly the non-cosmic background in *Chandra* and isolated unresolved components of the XRB in those bands which are only about ∼20% and ∼4% of the non-cosmic background contributions in those bands, respectively. The origin of the unresolved components is unknown. One possibility is stray light from sources outside the field of view. The HM06 total XRB intensity estimates in those bands are obtained by summing these unresolved components to the contributions from the resolved sources in the CDF data and from brighter sources using the $\log N - \log S$ derived by Vikhlinin et al. (1995), with different spectral slopes at different fluxes. Their 1–2 keV intensity is 4.6 ± 0.3 (in the above units), very similar to our adopted value. With their estimates of the total XRB intensity the total resolved fractions of the XRB are only $77 \pm 3\%$ and $80 \pm 8\%$ in the 1–2 keV and 2–8 keV bands respectively, which is lower than previous estimates, in particular in the softer band. We will discuss the origin of these differences in Sect. 5.4.

5.3. Contribution of different flux intervals to the X-ray background

X-ray intensities are shown in Table 6 for the observed flux intervals in the samples used here. For flux intervals with higher maximum fluxes they are chosen to "join" the observed intervals with the contribution from bright sources, which are also given in that table, as well as the XRB intensities from Moretti et al. (2003).

In Fig. 4 we have plotted the relative contribution of two flux intervals per decade to the total XRB intensity for the four

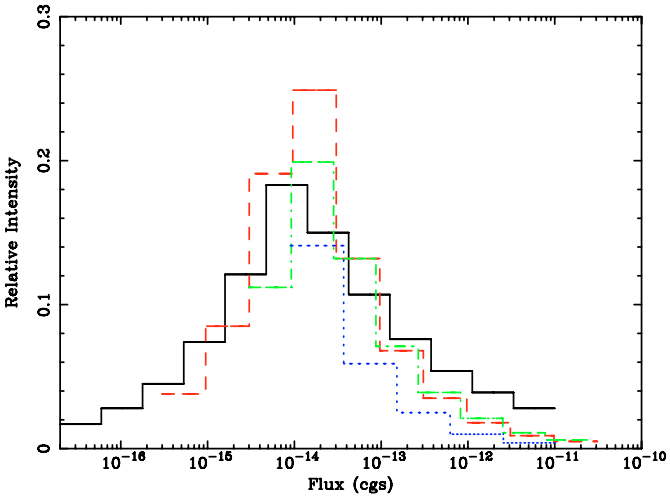

Fig. 4. Relative contribution to the "total" intensity from equally spaced logarithmic flux intervals using the best fit models in each band (see text): soft (solid line), hard (dashed), XID (dot-dashed) and ultra-hard (dotted).

default bands, assuming our best fit $\log N - \log S$. It is clear that the maximum contribution comes from fluxes around the break flux $\sim 10^{-14}$ cgs. The contribution from the bins in one decade around that value are close to 50% of the total in the soft and hard bands. In the ultra-hard band we do not reach deep enough to detect the break. Using the 5–10 keV band source counts of Hasinger et al. (2001) and Rosati et al. (2002) it is possible there could be a break just below $\sim 10^{-14}$ cgs.

The extrapolation of the soft and hard band $\log N - \log S$ to zero flux using our best fit model (see Table 6) does not saturate the XRB intensity, although in the soft band the total XRB intensity is within the intensities spanned by the uncertainties in the best fit $\log N - \log S$ parameters. This suggests that the possibility of a new dominant population at lower fluxes is still open, mainly in the hard band. Under the assumption that the fraction of truly diffuse XRB is negligible (the fluctuation analysis of Miyaji & Griffiths 2002 shows that the source counts continue growing in the soft band down to at least 7×10^{-18} cgs), it is possible to estimate the minimum slope of the source counts required to just saturate the XRB at zero flux, if the source counts steepened just below the minimum flux studied here. Those slopes are 1.85 and 1.84 in the soft and hard bands, respectively. Comparing these values to the observed slopes of the separate AGN and galaxy source counts in the CDF (Bauer et al. 2004), only the absorbed AGN (slope $\sim$ 1.62, versus 1.2–1.5 for the rest of the AGN estimates) come close to being able to saturate the soft XRB, while galaxies can do so with just about any estimate for their source counts slope (2.1–2.7) if they keep growing at the same rate below the resolved fluxes. The situation in the hard band is also the same, with the absorbed AGN (source counts slope 1.95, versus 1.4–1.5) being the only AGN population able to contribute the rest of the unresolved intensity, while the galaxy source counts estimates (slope 3–3.5) could easily fulfil this role. A similar conclusion is reached if a higher intensity for the XRB is adopted (HM06) since this would steepen the faint source counts slope required to saturate the XRB.

Even if the source counts re-steepened as discussed in the previous paragraph, it is clear that the maximum contribution to the XRB in the soft and hard bands (and probably also in the XID band, and perhaps also in the ultra-hard band) comes from sources with fluxes within a decade $\sim 10^{-14}$ cgs, where most of the AXIS sources in those bands lie. This is also true if the XRB intensity is higher than the value used here. Medium depth surveys with limiting fluxes close to that value are therefore crucial to understand the evolution of X-rays in the Universe, at least in the (relatively) soft bands considered here. Sources at lower fluxes and/or heavily obscured are of course much more important for the overall energy content of the XRB (Gilli et al. 2001; Fabian & Iwasawa 1999) since they mostly reside in harder X-rays, where the resolved fraction is much smaller (Worsley et al. 2004).

5.4. Resolved and unresolved components of the X-ray background

Comparison between HM06 results and ours (and previous) results involve an uncertainty concerning the different bands under consideration (0.5–2 keV vs. 1–2 keV and 2–8 keV vs. 2–10 keV). For the conversions from the 1–2 keV band to the soft band and vice versa, as well as the conversions from the 2–8 keV band to the 2–10 keV band, we have assumed power-law photon indices of 1.5 for the unresolved component (as fitted to the unresolved XRB spectrum by HM06), 1.43 for the resolved faint sources (again as fitted by HM06 to the summed spectrum of their resolved sources) and 2 for the resolved sources brighter than $\sim 10^{-14}$ cgs (Mateos et al. 2005). HM06 have excluded the areas around the sources in Alexander et al. (2003) from their study of the unresolved XRB, with 0.5–2 keV and 2–8 keV flux limits of 2.5×10^{-17} and 1.4×10^{-16} cgs respectively. Hence, HM06 define as unresolved any intensity coming from sources below those flux limits (or from a truly diffuse component).

An additional correction comes from the 2–8 keV band flux limits for the resolved sources of HM06, which they take from Alexander et al. (2003). This same sample was also the basis for the work of Bauer et al. (2004). We have already seen (Sect. 4.2) that those fluxes need to be decreased by 12% due to a change in the *Chandra* calibration, in addition to the correction due to the different bands, as discussed. Assuming a spectral slope of 1.43 and taking into account this flux correction, the flux limit in the 2–10 keV band becomes 1.6×10^{-16} cgs.

We compare in Table 7 the 0.5–2 keV, 1–2 keV and 2–10 keV X-ray intensity (from different origins and flux intervals) from HM06 and from the results of this and previous works. The error bars on our estimates of the intensities have been taken from the errors on the $\log N - \log S$ best fit parameters using the standard error propagation rules (Wall & Jenkins 2003). This has not been possible for the extrapolation to zero flux, since the expressions involve the natural logarithm of the lower limit of the interval. In this case we have used the values spanned by the uncertainties in the best fit $\log N - \log S$ parameters, as explained in Sect. 4.5.

The most noticeable difference is between the total soft XRB intensities, which are not compatible at the ~ 1-σ level, while the corresponding 1–2 keV intensities are compatible at 0.16-σ (see Sect. 5.2). This is because of the very different ways they have been obtained: our adopted value is from an extrapolation of the Moretti et al. (2003) 1–2 keV total XRB intensity assuming $\Gamma = 1.4$, while the HM06 estimate uses different contributions with different values of the photon index. Since the contribution from the brightest sources is almost half of the total and they have the steepest spectra, the "effective" spectral slope in the conversion of the HM06 XRB intensity from 1–2 keV to 0.5–2 keV is $\Gamma \sim 1.72$, much steeper than our assumed $\Gamma = 1.4$ and hence with a much larger contribution from the 0.5–1 keV interval. The HM06 resolved contribution also increases in the soft band with respect to the 1–2 keV band, but the resolved

Table 7. Comparison between the estimated X-ray intensities from HM06 and this and previous works, originating from different origins and flux intervals. The table is divided into three sections: the top one is for the soft band, the middle one for the 1–2 keV band and the bottom one for the hard band. In the middle section the conversion between 0.5–2 keV and 1–2 keV has been calculated in each flux interval using the photon indices given at the beginning of Sect. 5.4. The first two columns indicate the flux limits between which the intensity has been estimated. If the first value is missing the intensity is calculated from zero flux, while if the second one is missing the intensity is calculated up to infinity. The third column is the intensity from HM06 and the fourth column is the intensity from this work (or previous ones as indicated). The last three rows in each table section give the total intensity (as estimated directly by the sum of the values in the third column by HM06 and as estimated from previous works in the fourth column), the total intensity resolved into sources (with the stellar contribution subtracted, see Sect. 5.1) and the fraction of the total intensity resolved into sources.

0.5–2 keV			
Flux limits (cgs)		Intensity (10^{-12} cgs deg^{-2}) HM06	Here
	2.5×10^{-17}	1.8 ± 0.3	0.23 ± 0.09^a
2.5×10^{-17}	5.0×10^{-15}	2.4 ± 0.4	2.2 ± 0.4^a
5.0×10^{-15}	1.0×10^{-11}	4.2 ± 0.3	4.4 ± 1.4
1.0×10^{-11}		–	0.2^b
Total		8.4 ± 0.6	7.5 ± 0.4^c
Total resolved		6.6 ± 0.5	6.6 ± 1.7^e
Fraction resolved		0.79 ± 0.07	0.88 ± 0.23
1–2 keV			
Flux limits (cgs)		Intensity (10^{-12} cgs deg^{-2}) HM06	Here
	1.5×10^{-17}	1.0 ± 0.1	0.13 ± 0.05^a
1.5×10^{-17}	3.0×10^{-15}	1.5 ± 0.3	1.3 ± 0.2^a
3.0×10^{-15}	0.5×10^{-11}	2.1 ± 0.1	2.2 ± 0.7
0.5×10^{-11}		–	0.1^b
Total		4.6 ± 0.3	4.5 ± 0.2^c
Total resolved		3.6 ± 0.2	3.7 ± 0.7^e
Fraction resolved		0.78 ± 0.07	0.81 ± 0.16
2–10 keV			
Flux limits (cgs)		Intensity (10^{-12} cgs deg^{-2}) HM06	Here
	1.6×10^{-16}	4.2 ± 2.1	0.40 ± 0.04^a
1.6×10^{-16}	1.6×10^{-14}	9.5 ± 1.3	9.3 ± 0.4^a
1.6×10^{-14}	1.0×10^{-11}	7.0 ± 0.4	7.9 ± 1.5
1.0×10^{-11}	3.1×10^{-11}	–	0.09 ± 0.06
3.1×10^{-11}		–	0.4^d
Total		20.7 ± 2.5	20.2 ± 1.1^c
Total resolved		16.5 ± 1.3	17.3 ± 1.7^e
Fraction resolved		0.80 ± 0.11	0.86 ± 0.10

[a] Extrapolating our best fit $\log N - \log S$. [b] Schwope et al. (2000). [c] Moretti et al. (2003). [d] Piccinotti et al. (1982). [e] After subtracting the stellar contribution.

fraction increases only slightly because of the very similar effective spectral shapes of the resolved component and the XRB intensity. In contrast, our estimated resolved component is very similar to HM06, but our assumed XRB intensity in the 0.5–2 keV has a much flatter spectral shape, resulting in a smaller resolved fraction but still compatible within the errors.

We have also converted our different resolved contributions from the soft band to 1–2 keV using different spectral slopes for different flux intervals (as indicated at the beginning of this Section). The differences in the resolved components and in the resolved fraction with respect to HM06 are very small (see Table 7) and well within the mutual uncertainties.

In summary, in the soft band the difference in the total background intensity is just above 1-σ and mostly arises because of the different effective spectral shape assumed for the total XRB intensity between HM06 and most previous works. In contrast, the resolved intensities are very similar in HM06 and in our work.

A further source of uncertainty in the comparison of both XRB intensities is our extrapolation of the $\Gamma = 1.4$ XRB spectral shape below 1 keV where its real shape is not known. Assuming that the XRB spectrum steepens just below 1 keV with a power-law shape, we have estimated that $\Gamma = 2.2$ would be needed to produce our estimate of the HM06 soft XRB intensity from their 1–2 keV XRB intensity. This is difficult to accommodate, given the average slope of the faintest sources detected and of the unresolved component in the soft band ($\Gamma \sim 1.4$–1.5, HM06). Therefore the uncertainty in the <1 keV XRB spectral slope cannot fully account for the difference in the soft XRB intensities discussed above.

In the hard band there is a small, statistically insignificant discrepancy in the total background intensity. There is also agreement in the resolved component, where we estimate a slightly higher value but well within 1-σ. Our estimate of the bright source contribution in the hard band is fairly robust since the AMSS sources cover the same region of $\log N - \log S$ parameter space.

Extrapolating $\log N - \log S$ to zero flux we cannot saturate the unresolved component so either there is a diffuse component or the $\log N - \log S$ has to steepen again, somewhere below the current flux limits (see Tables 6, 7 and HM06).

6. Looking for source clustering

A survey to detect source clustering requires both depth (to achieve high angular density) and width (to minimise the possibility that a single structure biases the overall average). In practice, a compromise between those two conflicting requirements has to be achieved. The AXIS sample comprises 36 fields outside the Galactic plane and a relatively high source density (about 35 sources per field, at least in the soft and XID samples). In the following section we report on the implications of our sample for the angular distribution of sources in the sky.

6.1. Cosmic variance

The simplest test for source clustering is to compare the actual number of sources detected in each field, N_k, with the number expected, λ_k, from the best fit $\log N - \log S$ and the sky area of each individual field, Ω_k. This is similar to the traditional counts-in-cells method. In principle, if just one field (or a few fields) happen to look through strong cosmic structures the number of sources should be significantly different from the expected number for a random, uniform distribution as measured by the overall $\log N - \log S$.

Table 8. Information on the simulations for the angular correlation function together with fit results: Band is the band where the sources were selected, $N_{\rm pool}$ is the number of sources in the pool used for the bootstrap simulation (see text), N is number of sources selected in the real sample, $N_{\rm sim}$ is the number of simulations, χ^2_0 is the value of the χ^2 fit when using a "null" model, χ^2 is the best fit value for a power-law model (see Eq. 6) with the best fit parameters and their 1-σ uncertainty intervals given by the last two columns, $N_{\rm bin}$ is the number of bins used in the fit and $P(F)$ is the F-test probability that the improvement in the fit is significant (the smaller the $P(F)$ the higher the significance). The second row in each band corresponds to the best fit fixing γ to the "canonical" value 0.8.

Band	$N_{\rm pool}$	N	$N_{\rm sim}$	χ^2_0	χ^2	$N_{\rm bin}$	$P(F)$	θ_0 ($''$)	γ
Soft	1177	1131	1000	17.10	5.10	10	0.0079	19^{+7}_{-8}	$1.2^{+0.3}_{-0.2}$
					7.80	10	0.0096	6^{+2}_{-2}	$\equiv 0.8$
Hard	415	351	2500	8.47	7.33	10	0.5622	12^{+20}_{-12}	$1.1^{+2.8}_{-2.3}$
					7.47	10	0.3017	4^{+5}_{-4}	$\equiv 0.8$
XID	1301	1218	1000	16.00	5.30	10	0.0120	19^{+7}_{-8}	$1.3^{+0.4}_{-0.3}$
					8.80	10	0.0238	4^{+2}_{-2}	$\equiv 0.8$
UH	88	77	10 000	1.97	1.87	10	0.8119	0.7[a]	0.22[a]
					1.90	10	0.5759	8^{+26}_{-8}	$\equiv 0.8$
HR	250	225	10 000	3.60	1.10	10	0.0087	42^{+8}_{-12}	$3.9^{+2.5}_{-1.3}$
					3.22	10	0.3165	5^{+9}_{-5}	$\equiv 0.8$
Soft/3	392	380	2500	14.28	10.42	10	0.2835	35^{+11}_{-18}	$1.7^{+1.0}_{-0.6}$
					12.53	10	0.2912	7^{+7}_{-6}	$\equiv 0.8$

[a] Parameter unconstrained by the fit.

The statistics we have used to measure the deviation from such a random uniform distribution are the cumulative Poisson distributions:

$$\begin{aligned} P_{\lambda_k}(\geq N_k) &= \sum_{l=N_k}^{\infty} P_{\lambda_k}(l) \ \text{ if } N_k > \lambda_k \\ P_{\lambda_k}(\leq N_k) &= \sum_{l=0}^{N_k} P_{\lambda_k}(l) \ \text{ if } N_k < \lambda_k \end{aligned} \tag{3}$$

where $P_\lambda(l)$ is the Poisson probability of detecting l sources when the expected number of sources is λ. The cumulative distributions above give the probability of finding $\geq N_k$ (first row) or $\leq N_k$ (second row) sources when the expected number from the source counts is λ_k. This method is similar to the one used in Carrera et al. (1998) but in that work we used $P_\lambda(l)$ instead of the cumulative probabilities. We believe that the approach used here is a more conservative estimate to determine the likelihood of finding a number of sources in a field which is different from the expected value.

The maximum likelihood statistics for the whole sample is then

$$L' = -2 \sum_k P_{\lambda_k}(\geq N_k) - 2 \sum_{k'} P_{\lambda_{k'}}(\leq N_{k'}),$$

where k runs over the fields for which $N_k > \lambda_k$ and k' runs over the fields for which $N_{k'} < \lambda_{k'}$.

We have compared the observed L' values in each band with 10 000 simulated values, using the values of λ_k and Poisson statistics. The number of simulations with likelihood values above the observed ones were 1388, 4580, 778 and 4958 for the soft, hard XID and ultra-hard bands respectively. Nothing significant is found in the hard or ultra-hard samples, while some deviation below or at about the 90% significance level is found in the soft and XID bands. These results, although formally of low significance are sufficient to justify further and more detailed tests for clustering.

6.2. Angular correlation function

If cosmic structure is present in all (or most) fields, a test for significant deviations from the mean number of sources in each field from some overall average will not give significant results. We should look instead for evidence of sources tending to appear together in the sky with respect to an unclustered source distribution. The classic parametrisation for this effect is the angular correlation function, $W(\theta)$, which measures the excess probability of finding two sources in the sky at an angular distance θ with respect to a random uniform distribution (Peebles 1980):

$$\delta P = n^2 \delta\Omega_1 \delta\Omega_2 [1 + W(\theta)] \tag{4}$$

where δP is the probability of finding two objects in two small angular regions, $\delta\Omega_1$ and $\delta\Omega_2$, separated by an angle θ when the sky density of objects is n.

Since the angular separation is a projection in the sky of the real spatial separations of the sources at different redshifts, the underlying spatial clustering is somewhat blurred by this purely angular measurement. Unfortunately, the more powerful spatial clustering depends on having redshifts for a very high fraction of the sources, or at least knowing precisely the redshift distribution. Since none of these two conditions are fulfilled by any of the AXIS samples we have used the data presently at hand to study the angular correlation function.

There are several proposed methods to measure the angular correlation function, most of which look for an excess number of source pairs at a given angular separation, θ, with respect to a simulated, random "uniform" sample (Landy & Szalay 1993; Efstathiou et al. 1991). We have chosen the one proposed by Efstathiou et al. (1991),

$$W(\theta) = f \frac{DD}{DR} - 1 \tag{5}$$

where DD is the number of actual pairs of sources with angular separation θ, and DR is the number of pairs having one real and one randomly placed simulated source (see below) at the same separation, while f is a normalisation constant to take into account the different number of real and simulated sources. The error bars around each point are given by $\Delta W(\theta) = \sqrt{(1 + W(\theta))/DR}$ (Peebles 1980).

The "randomly placed" simulated sources have to follow as closely as possible the real distribution of the source detection sensitivity of the survey, giving a "flat" random sky against which to judge the presence (or otherwise) of significant overdensities at different angular separations. We have used bootstrap simulations by forming a pool of real sources with detection likelihoods higher than 15 (our standard value) in the band under study, irrespective of whether their count rates were above or below the sensitivity map of the corresponding field at the source positions. Then, keeping the number of simulated sources in each field equal to the real number of sources, N_k, we have extracted sources from this pool, keeping their count rates and their distances to the optical axis of the X-ray telescope but randomising their azimuthal angle around it. If the source had a count rate above the sensitivity map of the field under consideration at its "new" (X, Y) position, the source was kept in the simulated

sample, otherwise a new one is extracted until N_k valid simulated sources are found. In this way, the angular distribution of the simulated sources mimics the decline of the source detection sensitivity with off-axis angle. The number of random samples $N_{\rm sim}$ used in each band are shown in Table 8. They have been chosen so as to give a total of about a million simulated sources in each band.

Using this recipe, the normalisation constant f above is given by

$$f = \frac{\sum_k N_k\,(N_k - 1)}{2N_{\rm sim}\sum_k N_k^2},$$

N_k being the number of sources in field k and $N_{\rm sim}$ is the number of simulations.

If a positive correlation is present at angular scales comparable to the individual field size then the estimate of the mean surface density of objects from the survey is too high and this causes a negative bias in the angular correlation function known as the integral constraint (Basilakos et al. 2004). Given the complicated dependence of the sensitivity over the area of our survey we have corrected for this effect empirically, finding the angular correlation function that we would have detected in the absence of correlation via the average of $N_{\rm sim}$ simulated realisations of $W(\theta)$, where the real data were replaced by random samples simulated independently following the recipe in the previous paragraph. The triangles in Fig. 5 show these "zero points" at each angular scale which have been used to increase the corresponding observed $W(\theta)$, convolving the error bars using Gaussian statistics.

Applying Eq. (5) to the full sample results in a ∼3-σ significant bump at about 200 arcsec, which was also present in the simulations but at lower significance. The bump turned out to be present in only two fields, HD 111812 and HD 117555. A search in the literature revealed that both fields have stellar clusters in their field of view (Eggen & Iben 1989). Since we are mainly interested in extragalactic structure we have opted to exclude these two fields from all subsequent angular clustering analysis, leaving 34 fields.

The $W(\theta)$ values obtained in this fashion are shown in Fig. 5 as well as the corresponding best χ^2 fits to a power-law model

$$W(\theta) = (\theta/\theta_0)^{-\gamma}. \quad (6)$$

The best fit parameters for this model are given in Table 8. In this Table we also give the significance of the detection from an F-test, comparing the χ^2 value of the power-law model with a simple $W(\theta) = 0$, no-clustering model. The F-test suggests significant correlation in the soft and XID bands at the ∼99% level. The lack of significant detections in the two harder bands might be due to the lower number of sources with respect to the soft and XID bands (see below).

Gandhi et al. (2006) also found significant angular correlation in the XMM-LSS sample in the soft band with a similar slope, $\gamma = 1.2\pm0.2$, and a lower correlation length, $\theta_0 = 7\pm3$ arcsec, but still compatible with our result within ∼1-σ. Vikhlinin & Forman (1995) found $\gamma = 0.7 \pm 0.3$ and $\theta_0 = 4 \pm 3$ arcsec, again a lower correlation length than our results, but compatible within less than 1-σ with our $\gamma \equiv 0.8$ result. On the other hand, Basilakos et al. (2005) also found significant angular correlation in this band but with a higher correlation length, $\theta_0 = 10.4 \pm 1.9$ arcsec (with the canonical slope), just compatible with our results at about the 2-σ level. Basilakos et al. (2005) also used Limber's equation (Peebles 1980) to calculate the spatial correlation function from the angular correlation function, assuming several different AGN X-ray luminosity functions (since most X-ray sources at low flux levels are expected to be AGN). Their high correlation lengths are only compatible with AGN optical (e.g. Croom et al. 2002; Grazian et al. 2004) or X-ray correlation functions (Carrera et al. 1998; Akylas et al. 2000; Mullis et al. 2004) if the clustering is constant in physical coordinates, while optical QSO clustering seems instead to be constant in comoving coordinates (Croom et al. 2001, but see also Grazian et al. 2004 and Croom et al. 2005). Akylas et al. (2000) also found significant angular correlation in the soft band sources in the RASS-BSC, but at much higher angular distances (∼8°).

Correlation of hard band selected sources is not detected by Gandhi et al. (2006) (413 sources) and Puccetti et al. (2006) (205 sources). However, clustering is very significantly detected (>4σ) by Basilakos et al. (2004) (171 sources) with $\gamma = 1.2\pm0.3$ and $\theta_0 = 49^{+16}_{-25}$ arcsec. Clustering is also detected at similar significance by Yang et al. (2003), with $\theta_0 = 40 \pm 11$ arcsec (for $\gamma \equiv 0.8$) for 278 sources. This is somewhat surprising since the Basilakos et al. sample has less than half of the number of sources in Gandhi et al., and a similar number of sources to Puccetti et al., while the Yang et al. sample is again smaller than the Gandhi et al. sample. Our angular correlation length is compatible with the Basilakos et al. (2004) (and with the Puccetti et al.) result within 1-σ, but not with the Yang et al. correlation length. However, the F-test on the correlation function and the superior $P_\lambda(N)$ test (see below and Fig. 6) do not detect clustering. Again, our sample seems to give somewhat intermediate results in between those of Basilakos et al. (2004) and Yang et al. (2003) on one hand and Gandhi et al. (2006) and Puccetti et al. (2006) on the other.

Since each bin in $W(\theta)$ contains information from many pairs, perhaps involving the same real and simulated sources many times, it is at least debatable whether the hypothesis of independent bins underlying the χ^2 test applies in this case. To circumvent this problem we have applied a simple test for the significance of the correlation, using Poisson statistics to compare the expected number of pairs (at distances smaller or equal than each individual observed distance) in the absence of correlation ($\mu = \sum_{\theta'<\theta} DR(\theta')/f$) with the number of observed pairs ($N_\theta = \sum_{\theta'<\theta} DD(\theta')$). The quantity $1 - P_\mu(N_\theta)$ versus the angular distance θ is shown in Fig. 6 for each band. We estimated the "signal" in the absence of correlation in a similar way to the method used to quantify the integral constraint but here replacing the real data by randomly placed sources (see above). For each sample we have performed 10 000 simulations in this manner. Hence, for each angular scale and sample we have determined the distribution of the expected value of $1 - P_\mu(N_\theta)$ if the sources are not correlated. We show in Fig. 6 the median and the upper 99% and 99.9% percentiles of those distributions for each angular scale. The simulations show clearly that the detection significance is actually lower than the value given purely by Poisson statistics, when there are more than ∼1000 sources, as in the soft and XID bands where the 99% percentile is at around the Poisson 3-σ level. In the hard and ultra-hard bands the 99% percentile is close to the "right" Poisson position, albeit with large excursions.

Using the percentile values from the simulations we have found a >99% (but mostly <99.9%) significant detection of correlation in the angular positions in our soft sample at separations 200–700 arcsec. In the XID band the significance is lower, at just about 99% significance, with essentially one peak of higher significance at ∼300 arcsec. In contrast, no signal is found in either the hard or ultra-hard bands. The lack of significant detections in the two harder bands might be due to the lower number of sources with respect to the soft and XID bands.

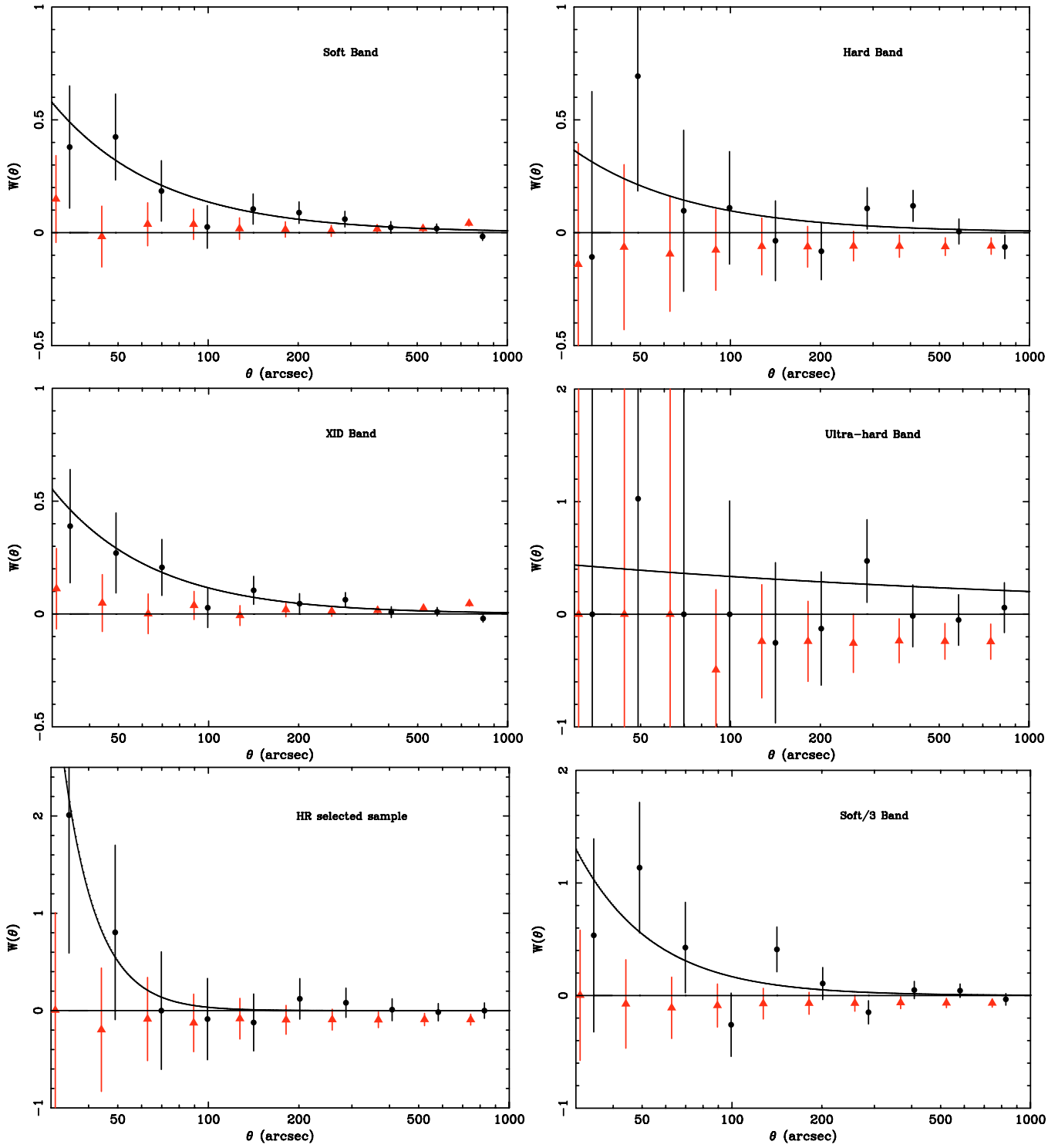

Fig. 5. $W(\theta)$ vs. θ for the soft (*top-left*), hard (*top-right*), XID (*middle-left*), and ultra-hard (*middle-right*) samples, for a hardness-ratio selected sample (*bottom-left*) and for a random selection of one third of the soft sources (*bottom-right*). The solid dots are the integral constraint-corrected observed values, the grey triangles show the "zero points" from the integral constraint (displaced to the left for clarity) and the solid lines are the best fit χ^2 fits to Eq. (6). The middle-right and two bottom panels have different scales on their Y-axis.

We have tested the influence of the number of sources on the detection of clustering, since we only detect clustering in the samples with more than 1000 sources. We rejected at random two of every three sources in the soft band sample and repeated both correlation tests and found that the clustering signal disappears (see Table 8, Figs. 5 and 6). We also repeated this test while keeping at random half and two thirds of the soft sources, only finding correlation at the 99% level in the last case. We conclude that clustering in the hard and ultra-hard bands may be as strong or stronger than clustering in the soft band but our relatively low number of sources prevents us from detecting it. This is consistent with the results of Gilli et al. (2005) who do not find any significant difference between the clustering properties of soft or hard X-ray selected sources in the CDF.

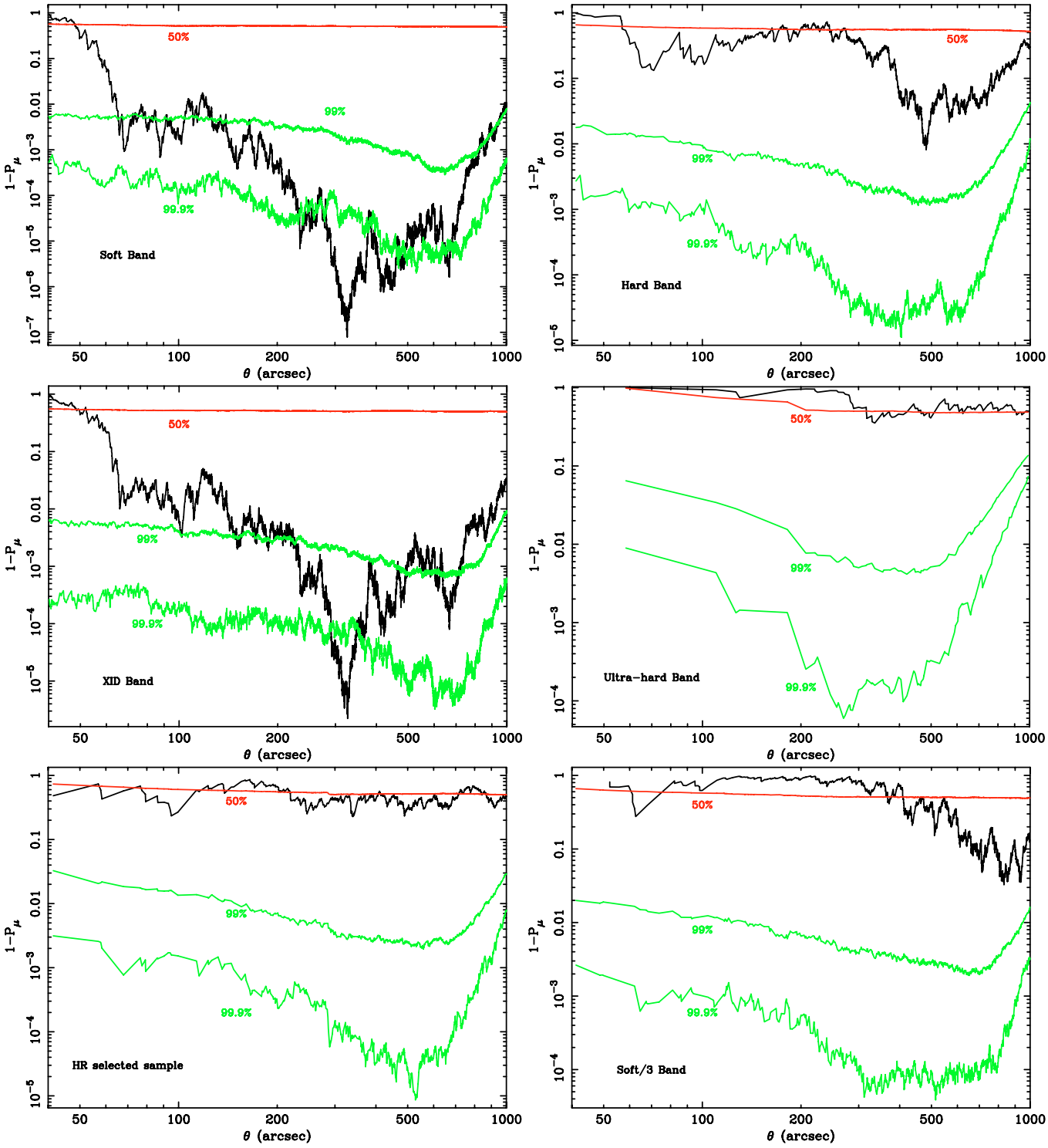

Fig. 6. $1 - P_\mu(N_\theta)$ vs. θ for the soft (*top-left*), hard (*top-right*), XID (*middle-left*), ultra-hard (*middle-right*) selected samples, for a hardness-ratio selected sample (*bottom-left*) and for a random selection of one third of the soft sources (*bottom-right*). The median (50%), 99% and 99.9% levels from random simulations are also shown (grey jagged lines). The *Y*-axis scaling is different in each panel and has been chosen for maximum clarity.

The significant clustering found for the $P_\mu(N_\theta)$ in the soft band corresponds to a broad bump between about 150 and 700 arcsec with "peaks" at about 300, 400 and 650 arcsec (the first two are significant even at the 99.9% level). These "peaks" also appear to be present in the XID band. While the increase in the number of real pairs giving rise to the broad bump is very gradual, the "peaks" must correspond to significant increases in relatively narrow ranges of angular distances. To investigate if these "peaks" come from a small number of fields in a particular region of the sky we divided the sample between the fields in the northern and southern Galactic hemispheres. The $1 - P_\mu(N_\theta)$ relation for these regions are shown in Fig. 7. Despite the lower significance of the results (expected because of the lower numbers of sources), the broad bump and peaks are still present in

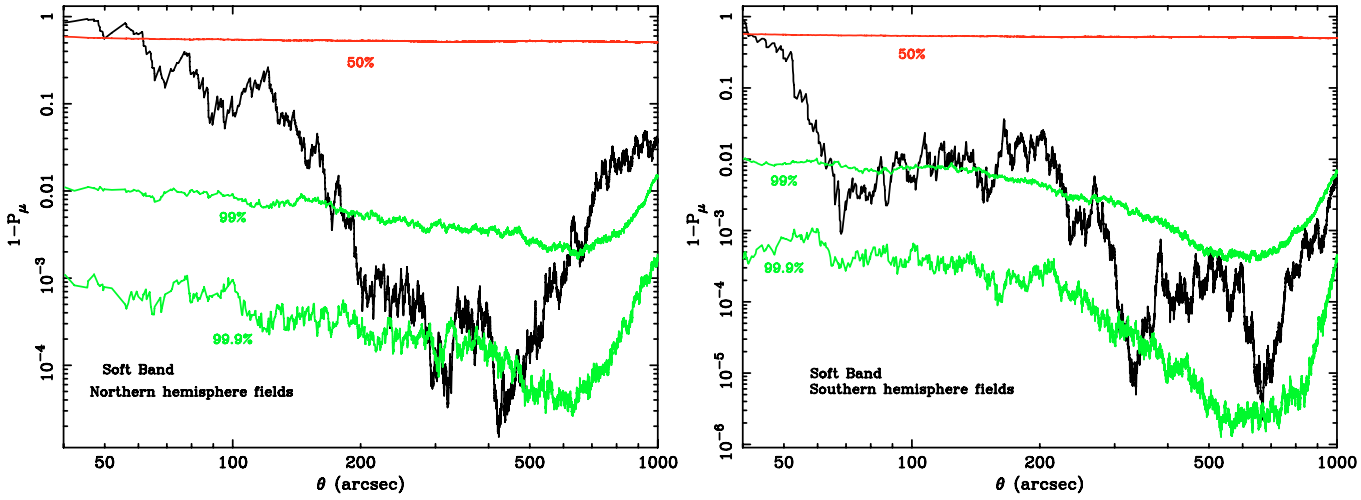

Fig. 7. $1 - P_\mu(N_\theta)$ vs. θ for the soft band and for the fields in the northern (*left*) and southern (*right*) Galactic hemispheres. The median (50%), 99% and 99.9% levels from random simulations are also shown (grey jagged lines).

the samples from each hemisphere with the ∼300 arcsec peak being common to both. The peak at 400 arcsec appears predominantly in the northern hemisphere and the peak at 650 arcsec occurs in the southern hemisphere. We have also repeated the analysis while excluding the two fields with obvious cluster emission (A1837 and A399) from the northern and southern Galactic hemisphere sub-samples respectively, finding no significant differences in the strength or position of the "peaks". As a further test, we have looked for this signal in the 7 deeper fields ($T_{\rm exp} > 40$ ks, ∼400 sources) and in the remaining 27 fields (∼800 sources), finding significant correlation only in the latter case and hence the signal is not introduced by a few deep fields.

A detailed discussion of the (cosmic or statistical) origin of these structures is outside the scope of this paper and will be discussed using a larger sample in a future paper. However, whatever the origin of the angular structure we have found, it must be relatively widespread over the survey area and/or the sky. We take this to mean that, if it has a real cosmic origin it must come from sources at $z \leq 1.5$, which is the peak of the redshift distribution of medium depth X-ray surveys (Barcons et al. 2007).

6.3. Angular correlation of a hardness ratio selected sample of sources

A low significance or absence of correlation in the hard band is somewhat surprising since most sources at the flux levels of our sample are AGN (Barcons et al. 2007), which are known to cluster strongly (both X-ray selected, Mullis et al. 2004; Yang et al. 2006, and optically selected, Croom et al. 2005). Furthermore, obscured AGN appear more commonly in hard X-ray selected samples (Della Ceca et al. 2006; Caccianiga et al. 2004; Della Ceca et al. 2004; Barcons et al. 2007).

Gandhi et al. (2006) have found that, despite the absence of significant angular correlation in their hard sample, if they select only the hardest spectrum sources (using the soft-to-hard hardness ratio) and they use lower significance sources, the significance of their correlation increases to $\sim 2-3\sigma$. They lowered their significance level in order to increase the number of sources in the tested sample. This significant correlation in only the hardest of the hard X-ray selected sources is a very intriguing and potentially interesting result.

We have performed a similar analysis, defining the same hardness ratio $HR = (H - S)/(H + S)$ where H and S are the 2–12 keV and 0.5–2 keV count rates respectively. We have selected the sources detected in either the soft or hard bands (in the sense explained in Sect. 2.4) which have $HR \geq -0.2$ (Gandhi et al. 2006).

The F-test seems to indicate correlation at >99% level (Table 8), but the superior Poisson method (Fig. 5) does not detect clustering on any angular scales, with the data being consistent with the median of the random simulations. We cannot thus confirm the results of Gandhi et al. (2006), despite having a slightly larger sample of sources (250 versus their 209). This is consistent with the results of Yang et al. (2006) who do not find any significant differences between the spatial clustering of sources with soft or hard spectra.

7. Conclusions

We present the results from AXIS (An *XMM-Newton* International Survey), which comprises 1433 distinct serendipitous X-ray sources detected above a likelihood of 15 (∼5-σ) in *XMM-Newton* EPIC pn observations in 36 different *XMM-Newton* observations at high Galactic latitude. We have defined sub-samples in four bands: 0.5–2 keV(soft, 1267 sources), 2–10 keV (hard, 397 sources), 0.5–4.5 keV (XID, 1359 sources) and 4.5–7.5 keV (ultra-hard, 91 sources). The first two being the "standard" X-ray bands, the third one chosen to span the energy range with the best sensitivity of that camera and the last one taking advantage of the unprecedented hard X-ray sensitivity of *XMM-Newton* above 4 keV. Given the distribution of exposure times of the fields selected for AXIS it will serve as a pathfinder for the X-ray and optical properties of the sources in large scale *XMM-Newton* catalogues (1XMM, 2XMM, ...).

Using count rates in the 5 standard *XMM-Newton* bands as low-resolution spectra we have fitted single power-laws to all sources in the XID and hard bands independently, in order to calculate source fluxes without assuming a constant spectrum (see Table 4). Our internal and external checks make us confident of the results using this technique. The average best fit power-law slope in the XID band is $\langle\Gamma\rangle \sim 1.8$, independent of the sample to which the sources belong, while the average is $\langle\Gamma\rangle \sim 1.5-1.6$ in the hard band.

We have constructed empirical sensitivity maps in all four bands taking into account the exposure maps, the background maps and the excluded regions (see Table 1). We have derived

sky coverage as a function of flux in each of these four bands, taking into account the distribution of spectral slopes of the sources. The total area covered is 4.8 deg^2 (see Fig. 1).

Our data have been combined with both wider and shallower (BSS/HBSS, Della Ceca et al. 2004, AMSS, Ueda et al. 2005) and narrower and deeper (CDF, Bauer et al. 2004) surveys to measure the X-ray source counts over as wide a flux range as possible, reaching 4 orders of magnitude in the soft band (∼2000 sources), ∼3 in the hard and XID bands (∼800 and ∼1800 sources, respectively) and a bit more than 1 in the (largely unexplored) ultra-hard band (∼140 sources). The data from different observatories and instruments are mutually compatible so allowing a joint analysis of the source counts.

We have performed maximum likelihood fits to a broken power-law model for the $\log N - \log S$ in each of the four bands (see Table 5). We have found that fits to the source counts using fixed spectral slopes produce similar results to those using individual source spectral slopes (as we have done here) but give rise to larger error bars. The source counts in the soft, hard and XID bands show breaks at fluxes $\sim 10^{-14}$ cgs. Detailed examination of the ratios between the data and this simple model in the soft and XID band do not show any significant differences, while in the hard band there seems to be evidence for a further flux break at $\sim 3 \times 10^{-15}$ cgs and several changes of slope. Since this is only present in the hard band, it is difficult to assess whether this behaviour is due to an over simple characterisation of contributions from different populations at different redshifts or to calibration uncertainties. Future large scale *XMM-Newton* catalogues (such as 2XMM) will be useful for addressing this question. The best fit model parameter values are compatible with previous smaller or similar surveys, but our combination of large number of sources and wide flux coverage produce in general smaller uncertainties in the best fit parameters.

We have used our best fit $\log N - \log S$ parameters to calculate both the total resolved fraction of the XRB (including the contribution from sources at bright fluxes, see Table 6) and the relative contribution of different flux bins to the XRB (see Fig. 4). We have used the estimates of the average XRB intensity in the soft and hard bands from Moretti et al. (2003) and translated them to the XID and ultra-hard bands using $\Gamma = 1.4$ (Marshall et al. 1980). The total resolved fraction down to the lowest fluxes of the combined sample reaches 87% in the soft band and 85% in the hard band, where we have been able to reach deep fluxes using pencil beam surveys (Bauer et al. 2004), but is only ∼60% in the XID band and about 25% in the ultra-hard band. The total intensity produced by extrapolating our best fit soft and hard $\log N - \log S$ to zero flux is insufficient to saturate the XRB intensity. Assuming a second flux break just below our minimum detected fluxes, we have estimated the minimum slope below this break necessary to reproduce the whole XRB with discrete sources, obtaining 1.85 (1.84) in the soft (hard) band. Comparing these slopes with those of the fainter galaxy and AGN source counts from the CDF (Bauer et al. 2004), we show that galaxies could easily provide this re-steepening, while among AGN only perhaps the absorbed cases could possibly do so.

The maximum fractional contribution to the XRB in the soft, hard and XID bands comes from sources within a decade of 10^{-14} cgs (which is about where the break flux for the broken power-law occurs). This fractional contribution reaches about 50% of the total in the soft and hard bands. Medium depth surveys such as AXIS (and indeed the 1XMM catalogue and its successor 2XMM) are therefore crucial to understand the evolution of the X-ray emission in the Universe, at least up to 10 keV.

Hickox & Markevitch (2006) have recently re-estimated the soft and hard XRB intensities using CDF data, finding lower resolved fractions of the XRB than our (and previous) estimates. We have found that the difference between our results in the soft band (where it is highest) is only at the ∼1-σ level and is mainly due to the different ways in which the total XRB intensity is calculated. HM06 add different contributions at different fluxes, which produces an "effective" spectral shape of the XRB ($\Gamma \sim 1.8$) which is much steeper than the "canonical" XRB spectral slope of $\Gamma = 1.4$ (which we have assumed). We have shown that the difference between these estimates of the soft XRB intensity cannot be removed just by relaxing our assumption. The HM06 intensity from resolved sources is very similar to ours. Converting our results to 1–2 keV the difference with HM06 all but vanishes.

After excluding two fields in which there is evidence for the presence of stellar clusters we used the AXIS sources to study the presence of cosmological structure in the X-ray sky, through the cosmic variance in the number of sources per field and the distribution of the angular separations of the sources. The former is in principle more sensitive to the presence of significant over-densities in a few fields while the latter detects any overall angular clustering of sources. No cosmic variance is detected at all in the hard and ultra-hard bands while some signal at about the 90% level is present in the soft and XID bands, probably because they are the ones with the larger number of sources.

Angular clustering is studied in two ways. The first is the angular correlation function, $W(\theta)$. Using this method we detect signal at about the 99% level in the soft and XID bands but not in the hard and ultra-hard bands (Table 8 and Fig. 5). The strength of the clustering signal we have found is intermediate between those of previous results (e.g. Gandhi et al. 2006; Basilakos et al. 2004, 2005; Vikhlinin & Forman 1995). Formally, a more appropriate method using Poissonian statistics detects clustering at the 99–99.9% level in the soft and XID samples, but not in the hard or ultra-hard bands (Fig. 6). Repeating the test for a random, 1-in-3 selected sample of soft sources completely removes the clustering signal, which we take to imply that there might be a "real" angular clustering among hard sources which we have failed to detect due to the smaller number of sources. Dividing the soft sample into several sub-samples reveals that the signal is widespread over the sky and not limited to a few deep fields. This means that if it has a cosmic origin it must come from $z \leq 1.5$, the peak of the redshift distribution of medium flux X-ray surveys (Barcons et al. 2007). We cannot confirm the detection of a signal among hard-spectrum hard sources reported by Gandhi et al. (2006).

Acknowledgements. This research has made use of the NASA/IPAC Extragalactic Database (NED; which is operated by the Jet Propulsion Laboratory, California Institute of Technology, under contract with the National Aeronautics and Space Administration) and of the SIMBAD database (operated by CDS, Strasbourg, France). Financial support for this work was provided by the Spanish Ministerio de Educación y Ciencia under projects ESP2003-00812 and ESP2006-13608-C02-01. This research has made use of the USNO-A2.0 catalogue, maintained at the U.S. Naval Observatory. SM, MP, MW, JT and SR acknowledge financial support for this research from PPARC. RDC and TM received partial financial support from the Italian Space Agency under contract ASI-INAF n. I/023/05/0.

References

Akylas, A., Georgantopoulos, I., & Plionis, M. 2000, MNRAS, 318, 1036
Alexander, D., Bauer, F. E., Brandt, W. N., et al. 2003, AJ, 126, 539
Arnaud, K. 1996, Astronomical Data Analysis Software and Systems V., ed. G. Jacoby, & J. Barnes, ASP Conf. Ser., 101, 17
Baldi, A., Molendi, S., Comastri, A., et al. 2002, ApJ, 564, 190

Barcons, X., Mateos, S., & Ceballos, M. T. 2000, MNRAS, 311, 456
Barcons, X., Carrera, F. J., Watson, M. G., et al. 2002, A&A, 382, 522
Barcons, X., Carrera, F. J., & Ceballos, M. T. 2006, ESA-SP, 604, 789
Barcons, X., Carrera, F. J., et al. 2007, submitted to A&A
Basilakos, S., Georgakakis, A., Plionis, M., & Georgantopoulos, I. 2004, ApJ, 607, L79
Basilakos, S., Plionis, M., Georgakakis, A., & Georgantopoulos, G. 2005, MNRAS, 356, 183
Bauer, F. E., Alexander, D. M., Brandt, W. N., et al. 2004, AJ, 128, 2048
Caccianiga, A., Severgnini, P., Braito, V., et al. 2004, A&A, 416, 901
Cagnoni, I., Della Ceca, R., & Maccacaro, T. 1998, ApJ, 493, 54
Cappelluti, N., Hasinger, G., Brusa, M., et al. 2007, ApJS, in press [arXiv:astro-ph/0701196]
Carrera, F. J., Barcons, X., Fabian, A. C., et al. 1998, MNRAS, 299, 229
Civano, F., Comastri, A., & Brusa, M. 2005, MNRAS, 358, 693
Cowie, L. L., Garmire, G. P., Bautz, M. W., et al. 2002, ApJ, 566, L5
Croom, S. M., Shanks, T., Boyle, B. J., et al. 2001, MNRAS, 325, 483
Croom, S. M., Boyle, B. J., Loaring, N. S., et al. 2002, MNRAS, 335, 459
Croom, S. M., Boyle, B. J., Shanks, T., et al. 2005, MNRAS, 356, 415
De Luca, A., & Molendi, S. 2004, A&A, 419, 837
Della Ceca, R., Castelli, G., Braito, V., Cagnoni, I., & Maccacaro, T. 1999, ApJ, 524, 674
Della Ceca, R., Maccacaro, T., Caccianiga, A., et al. 2004, A&A, 428, 383
Della Ceca, R., Caccianiga, A., Severgnini, P., et al. 2006, ESA-SP, 604, 783
Dickey, J. M., & Lockman, F. J. 1990, ARA&A, 28, 215
Eddington, A. S. 1913, MNRAS, 73, 359
Efstathiou, G., Bernstein, G., Tyson, J. A., Katz, N., & Guhathakurta, P. 1991, ApJ, 380, L47
Eggen, O. J., & Iben, I. 1989, AJ, 97, 431
Ehle, M., Breitfellner, M., González-Riestra, R., et al. 2005, *XMM-Newton* Users' Handbook, ESA
Fabian, A. C., & Barcons, X. 1992, ARA&A, 30, 429
Fabian, A. C., & Iwasawa, K. 1999, MNRAS, 303, L34
Gabriel, C., Denby, M., Fyfe, D. J., et al. 2004, in Astronomical Data Analysis software and Systems XIII, ed. F. Ochsensbein, M. Allen, & D. Egret, ASP Conf. Ser., 314, 759
Gandhi, P., Garcet, O., Disseau, L., et al. 2006, A&A, 457, 393
Giacconi, R., Gursky, H., Paolini, F. R., & Rossi, B. B. 1962, Phys. Rev. Lett., 9, 439
Giacconi, R., Rosati, P., Tozzi, P., et al. 2001, ApJ, 551, 624
Giacconi, R., Zirm, A., Wang, J., et al. 2002, ApJS, 139, 369
Gilli, R., Salvati, M., & Hasinger, G. 2001, A&A, 366, 407
Gilli, R., Daddi, E., Zamorani, G., et al. 2005, A&A, 430, 811
Grazian, A., Negrello, M., Moscardini, L., et al. 2004, AJ, 127, 592
Hasinger, G., Burg, R., Giacconi, R., et al. 1998, A&A, 329, 482
Hasinger, G., Altieri, B., Arnaud, M., et al. 2001, A&A, 365, L45
Hasinger, G., Cappelluti, N. Brunner, H., et al. 2007, ApJS, in press [arXiv:astro-ph/0612311]
Hickox, R. C., & Markevitch, M. 2006, ApJ, 645, 95
Hornschemeier, A. E., Bauer, F. E., Alexander, D. M., et al. 2003, AJ, 126, 575
Kim, D.-W., Cameron, R. A., Drake, J. J., et al. 2004, ApJS, 150, 19
La Franca, F., Fiore, F., Comastri, A., et al. 2005, ApJ, 635, 864
Landy, S. D., & Szalay, A. 1993, ApJ, 412, 64
Loaring, N., Dwelly, T., Page, M. J., et al. 2005, MNRAS, 362, 1371
Lumb, D. H., Warwick, R. S., Page, M., & De Luca, A. 2002, A&A, 389, L93
Marshall, F. E., Boldt, E. A., Holt, S. S., et al. 1980, ApJ, 235, 4
Mateos, S., Barcons, X., Carrera, F. J., et al. 2005, A&A, 433, 855
Miyaji, T., & Griffiths, R. E. 2002, ApJ, 564, L5
Moretti, A., Campana, S., Lazzati, D., & Tagliaferri, G. 2003, ApJ, 588, 696
Mullis, C. R., Henry, J. P., Gioia, I. M., et al. 2004, ApJ, 617, 192
Page, M. J., Mittaz, J. P. D., & Carrera, F. J. 2000, MNRAS, 318, 1073
Peebles, P. J. E. 1980, The large-scale structure of the universe (Princeton University Press), 435
Piccinotti, G., Mushotzky, R. F., Boldt, E. A., et al. 1982, ApJ, 253, 485
Pierre, M., Valtchanov, I., Altieri, B., et al. 2004, J. Cosm. Astropart. Phys., 9, 11
Puccetti, S., Fiore, F., D'Elia, V., et al. 2006, A&A, 457, 501
Rosati, P., Tozzi, P., Giacconi, R., et al. 2002, ApJ, 566, 667
Schwope, A., Hasinger, G., Lehmann, I., et al. 2000, AN, 321, 1
Setti, G., & Woltjer, L. 1989, A&A, 224, L21
Sołtan, A. 1982, MNRAS, 200, 115
Strüder, L., Briel, U., Dennerl, K., et al. 2001, A&A, 365, L18
Tedds, J. A., Page, M. J., et al. 2007, in preparation
Turner, M. J. L., Abbey, A., Arnaud, M., et al. 2001, A&A, 365, L27
The First *XMM-Newton* Serendipitous Source Catalogue, *XMM-Newton* Survey Science Centre, 2003 (http://xmmssc-www.star.le.ac.uk/)
Ueda, Y., Akiyama, M., Ohta, K., & Miyaji, T. 2003, ApJ, 598, 886
Ueda, Y., Ishisaki, Y., Takahashi, T., Makishima, K., & Ohashi, T. 2005, ApJS, 161, 185
Ueda, Y., et al. 2007, in preparation
Vikhlinin, A., & Forman, W. 1995, ApJ, 455, L109
Vikhlinin, A., Forman, W., Jones, C., & Murray, S. 1995, ApJ, 451, 564
Wall, J. V., & Jenkins, C. R. 2003, Practical Statistics for Astronomers (Cambridge University Press)
Worsley, M. A., Fabian, A. C., Barcons, X., et al. 2004, MNRAS, 352, l28
Worsley, M. A., Fabian, A. C., Bauer, F. E., et al. 2006, MNRAS, 368, 1735
Yang, Y., Mushotzky, R. F., Barger, A. J., et al. 2003, ApJ, 585, L85
Yang, Y., Mushotzky, R. F., Barger, A. J., & Cowie, L. L. 2006, ApJ, 645, 68
Zamorani, G. Gioia, I. M., Maccacaro, T., & Wolter, A. 1988, A&A, 196, 39

Online Material

Table 1. Basic data for the 36 fields in the AXIS survey: including the target name, the *XMM-Newton* OBS_ID number of the pn dataset used, the RA and Dec of the field centre, the "clean" exposure time and the filter used for the pn camera, the Galactic column density in the direction of the field (Dickey & Lockman 1990) and, where applicable, the centre and radius of the circular exclusion area for the target, the width of the OOT exclusion area and the centre and radius of an additional exclusion area around bright/extended sources.

Target name	OBS_ID	RA (J2000)	Dec (J2000)	T exp (s)	Filter	$N_{H,Gal}$ (10^{20} cm^{-2})	RA (J2000)	Dec (J2000)	R (")	OOT (")	RA (J2000)	Dec (J2000)	R' (")
A2690	0125310101	00:00:30.30	−25:07:30.00	21586.7	Medium	1.84	00:00:21.2	−25:08:12.18	20	0	-	-	0
Cl0016+1609[a]	0111000101	00:18:33.00	+16:26:18.00	29149.3	Medium	4.07	00:18:33.2	+16:26:07.97	148	0	-	-	0
G133-69pos_2[a]	0112650501	01:04:00.00	−06:42:00.00	18080.0	Thin	5.19	-	-	0	0	-	-	0
G133-69Pos_1[a]	0112650401	01:04:24.00	−06:24:00.00	20000.0	Thin	5.20	-	-	0	0	-	-	0
PHL1092	0110890501	01:39:56.00	+06:19:21.00	16180.0	Medium	4.12	01:39:55.8	+06:19:19.67	88	40	01:40:09.0	+06:23:27.67	68
SDS-1b[a,d]	0112371001	02:18:00.00	−05:00:00.00	43040.0	Thin	2.47	-	-	0	0	-	-	0
SDS-3[a,d]	0112371501	02:18:48.00	−04:39:00.00	14927.9	Thin	2.54	-	-	0	0	-	-	0
SDS-2[a,d]	0112370301	02:19:36.00	−05:00:00.00	40673.0	Thin	2.54	-	-	0	0	-	-	0
A399[a,c]	0112260201	02:58:25.00	+13:18:00.00	14298.7	Thin	11.10	02:57:50.2	+13:03:20.88	272	0	-	-	0
Mkn3[a,c]	0111220201	06:15:36.30	+71:02:04.90	44506.1	Medium	8.82	06:15:36.6	+71:02:15.95	76	32	-	-	0
MS0737.9+7441[a,e]	0123100201	07:44:04.50	+74:33:49.50	20209.3	Thin	3.51	07:44:04.3	+74:33:54.56	120	40	-	-	0
S5 0836+71[a]	0112620101	08:41:24.00	+70:53:40.70	25057.3	Medium	2.98	08:41:24.3	+70:53:41.06	160	52	-	-	0
PG0844+349	0103660201	08:47:42.30	+34:45:04.90	9783.5	Medium	3.28	08:47:42.9	+34:45:03.27	200	40	-	-	0
Cl0939+4713[a]	0106460101	09:43:00.10	+46:59:29.90	43690.0	Thin	1.24	09:43:01.8	+46:59:44.37	160	0	-	-	0
B21028+31[a]	0102040301	10:30:59.10	+31:02:56.00	23236.0	Thin	1.94	10:30:59.3	+31:02:56.08	140	72	-	-	0
B21128+31[a]	0102040201	11:31:09.40	+31:14:07.00	13799.8	Thin	2.00	11:31:09.6	+31:14:06.02	140	44	-	-	0
Mkn205[a,e]	0124110101	12:21:44.00	+75:18:37.00	17199.6	Medium	3.02	12:21:43.8	+75:18:39.08	140	36	-	-	0
MS1229.2+6430[a,e]	0124900101	12:31:32.32	+64:14:21.00	28700.0	Thin	1.98	12:31:31.2	+64:14:18.06	140	40	-	-	0
HD111812[b]	0008220201	12:50:42.56	+27:26:07.70	37338.8	Thick	0.90	12:51:42.6	+27:32:23.27	168	40	-	-	0
NGC4968	0002940101	13:07:06.10	−23:40:43.00	4898.7	Medium	9.14	13:07:06.3	−23:40:33.23	40	0	-	-	0
NGC5044	0037950101	13:15:24.10	−16:23:06.00	20030.0	Medium	5.03	13:15:24.2	−16:23:08.53	340	0	-	-	0
IC883	0093640401	13:20:35.51	+34:08:20.50	15849.4	Medium	0.99	13:20:35.4	+34:08:21.37	48	0	13:20:54.4	+33:55:17.26	104
HD117555[a,b]	0100240201	13:30:47.10	+24:13:58.00	33225.4	Medium	1.16	13:30:47.8	+24:13:51.07	160	40	-	-	0
F278	0061940101	13:31:52.37	+11:16:48.70	4648.3	Thin	1.93	13:31:52.4	+11:16:43.88	48	0	-	-	0
A1837[a]	0109910101	14:01:34.68	−11:07:37.20	45361.3	Thin	4.38	14:01:36.5	−11:07:43.14	440	0	-	-	0
UZLib[a]	0100240801	15:32:23.00	−08:32:05.00	23391.2	Medium	8.97	15:32:23.4	−08:32:05.32	140	40	-	-	0
FieldVI	0067340601	16:07:13.50	+08:04:42.00	9634.0	Medium	4.00	-	-	0	0	-	-	0
PKS2126-15[a]	0103060101	21:29:12.20	−15:38:41.00	16150.0	Medium	5.00	21:29:12.1	−15:38:40.44	120	40	-	-	0
PKS2135-14[a,f]	0092850201	21:37:45.45	−14:32:55.40	28484.3	Medium	4.70	21:37:45.1	−14:32:55.22	120	44	-	-	0
MS2137.3-2353	0008830101	21:40:15.00	−23:39:41.00	9880.0	Thin	3.50	21:40:15.1	−23:39:39.32	140	48	-	-	0
PB5062[a]	0012440301	22:05:09.90	−01:55:18.10	28340.9	Thin	6.17	22:05:10.3	−01:55:20.38	140	40	-	-	0
LBQS2212-1759[a]	0106660101	22:15:31.67	−17:44:05.00	90892.5	Thin	2.39	-	-	0	0	-	-	0
PHL5200[a]	0100440101	22:28:30.40	−05:18:55.00	43278.5	Thick	5.26	22:28:30.4	−05:18:53.12	16	0	-	-	0
IRAS22491-1808[a]	0081340901	22:51:49.49	−17:52:23.20	19867.2	Medium	2.71	22:51:49.4	−17:52:25.02	32	0	-	-	0
EQPeg[a]	0112880301	23:31:50.00	+19:56:17.00	12200.0	Thick	4.25	23:31:52.7	+19:56:18.46	160	48	-	-	0
HD223460	0100241001	23:49:41.00	+36:25:33.00	6699.0	Thick	8.25	23:49:40.8	+36:25:32.56	172	40	23:50:02.0	+36:25:36.36	116

[a] Fields belonging to the XMS.
[b] Fields excluded from the angular correlation studies.
[c] `eposcorr` astrometric correction failed in these fields.
[d] In common with SXDS (Ueda et al. 2006).
[e] In common with HELLAS2XMM (Baldi et al. 2002).
[f] Same area as one ChaMP field (Kim et al. 2004).

Appendix A: Empirical sensitivity maps

The present version of `esensmap` (the SAS task to calculate sensitivity maps for the EPIC cameras on board *XMM-Newton*) assumes pure Poissonian statistics to evaluate the detection sensitivity at different positions in the field of view. Since the detection of the sources and the determination of their parameters is a complicated process which needs to take into account how well the profile of the count rates matches the PSF, the result is bound to deviate from the naïve assumption of pure Poissonian statistics.

We have followed an empirical approach looking for a simple relationship between the observed EPIC pn count rates of the detected sources in each band, *cr* (in cts/s, columns `RATE` in the SAS source lists), and the pure Poissonian count rate, *crpoisim* (in cts/s), as calculated from the total number of background counts, *bgdim*, within a circle of radius *cutrad* (related to the column labelled `CUTRAD` in the SAS source lists and given in units of 4″ pixels) around the source position, the detection likelihood of the source, L (columns labelled `DET_ML` in the SAS source lists), and the average value of the exposure map (in seconds) within that radius *expim*, such that

$$-\log(P_{bgdim}(> (bgdim + crpoisim \times expim)) = L \qquad \text{(A.1)}$$

where $P_\lambda(>N)$ is as defined in Eq. (3).

The values of `CUTRAD` are in principle different for each source in each field since they are chosen by `emldetect` to maximise the signal-to-noise ratio for source detection. We have found that there is no significant correlation between `CUTRAD` and either the off-axis angle of the source, `RATE` or `BG_MAP` (the average background value in counts per pixel within the extraction circle) and therefore we have adopted for *cutrad* in each band the average of `CUTRAD` for the sources having L between 8 and 20 in that band. We have checked that there is no significant difference in the goodness of fits below when using either the actual `CUTRAD` value for each source or the average *cutrad*.

expim above is the average of the exposure map within a circle of radius *cutrad* around the X-ray source positions. The exposure maps for the single bands are PPS products. We have created exposure maps for the composite bands using the SAS task `eexpmap` which generates exposure maps for the energy in the middle of the PI interval and could be inaccurate for wide bands. To assess the effect of this approximation we have also calculated "average" exposure maps in the composite bands by weighting the single band exposure maps with the counts in the images, pixel by pixel. Again, there are no significant differences between the results from the two different types of exposure maps.

The background files, however, are not PPS products. We have generated them from the individual and composite bands using the SAS task `esplinemap` which excludes areas around the sources in an input source list and fits the remaining background using a spline (with 16 nodes in our case). We have then calculated *bgdim* by summing the values of the background image over a circle of radius *cutrad*.

We show in Fig. A.1 plots of `RATE` versus *crpoisim* for the single and composite bands along with the best linear fit model, `RATE`$= LI \times crpoisim$, for sources having $8 \le L \le 20$ in each band. The best fit *LI* along with the values of *cutrad* for each band are given in Table A.1. From the number of sources in each fit and the values of χ^2 it is clear that the fits are quite good and more sophisticated models are not needed. The values of *LI* are all within ∼10% of 1, implying that the correction is small, as expected, but from the improvement of the χ^2 values in using $LI \equiv 1$ (which is equivalent to `RATE`$\equiv$ *crpoisim*) we conclude that it is also highly significant.

Table A.1. Summary of the results of the linear fits of *crpoisim* to `RATE`: Band is the band used for the fit, *cutrad* is the source extraction radius (in units of 4″ pixels), *LI* is the best fit multiplying constant, N is the number of sources in the fit, χ^2_{LI} is the χ^2 value of the best linear fit, χ^2_0 is the χ^2 of the fit to $LI \equiv 1$ and $P(F)$ the F-test probability of allowing $LI \neq 1$ and not being a significant improvement to the fit.

Band	*cutrad* (pixels)	*LI*	N	χ^2_{LI}	χ^2_0	$P(F)$
1	5.12	1.14	284	104.5	185.5	$<10^{-6}$
2 (soft)	5.08	1.10	653	140.1	226.0	$<10^{-6}$
3	5.15	1.14	414	105.7	208.4	$<10^{-6}$
4 (ultra-hard)	5.49	1.14	127	25.7	56.2	$<10^{-6}$
5	5.86	1.15	16	1.7	5.5	$<10^{-4}$
9 (XID)	5.04	1.02	722	141.0	145.2	$<10^{-5}$
3-5 (hard)	5.18	0.89	243	176.2	237.8	$<10^{-6}$

The recipe for creating a sensitivity map is then:

1. Create background and exposure maps.
2. Choose a likelihood value, L, for the significance of the detections. This recipe has only been tested for $8 \le L \le 20$ but in principle it could be valid for likelihood values outside this interval.
3. Choose a source extraction radius, *cutrad*, appropriate for the band you are interested in (Table A.1).
4. For each pixel (X, Y) in an input image:
   (a) Calculate the sum of the values of the pixels in the background map whose centres are within *cutrad* of (X, Y): *bgdim*
   (b) Calculate the average of the values of the pixels in the exposure map whose centres are within *cutrad* of (X, Y): *expim*
   (c) Find *ctspoisim* such that $-\log(P_{bgdim}(> (ctspoisim + bgdim))) = L$
   (d) Calculate $sens(X, Y) = ctspoisim/expim \times$LI.
5. $sens(X, Y)$ is our empirical estimate of the typical count rate of a source at (X, Y) detected with likelihood L.

Appendix B: Evaluating the count rate spectral fit

To check the validity of our procedure we have performed both internal and external tests to evaluate the count rate spectra fit. The simplest internal check is to simulate sources with a single spectral slope ($\Gamma = 2$ in our case), fit them and then compare the output slope values to the input value. We have kept the total (0.5–10 keV) count rates of the sources fixed to the observed count rates and simulated the count rates in each band using a Poissonian deviation from the expected number of counts for the fixed slope and the exposure times, $T_{\rm exp}$, in Table 1. The errors in the simulated count rates, (ΔCR), were more challenging to estimate. Using simply $\Delta CR = \sqrt{CR/T_{\rm exp}}$ would not be adequate because it does not include the contribution from the background subtraction and because the statistics of the source detection by `emldetect` are very close to but not exactly Poissonian. We have used the selected sources to look for an empirical relationship between the observed ΔCR and the naive $\sqrt{CR/T_{\rm exp}}$. We have found that a linear relationship is a good visual fit with the parameters given in Table B.1. This is the recipe we have used to simulate the errors in the count rates in our simulations. The weighted averages of the fitted slopes are given in

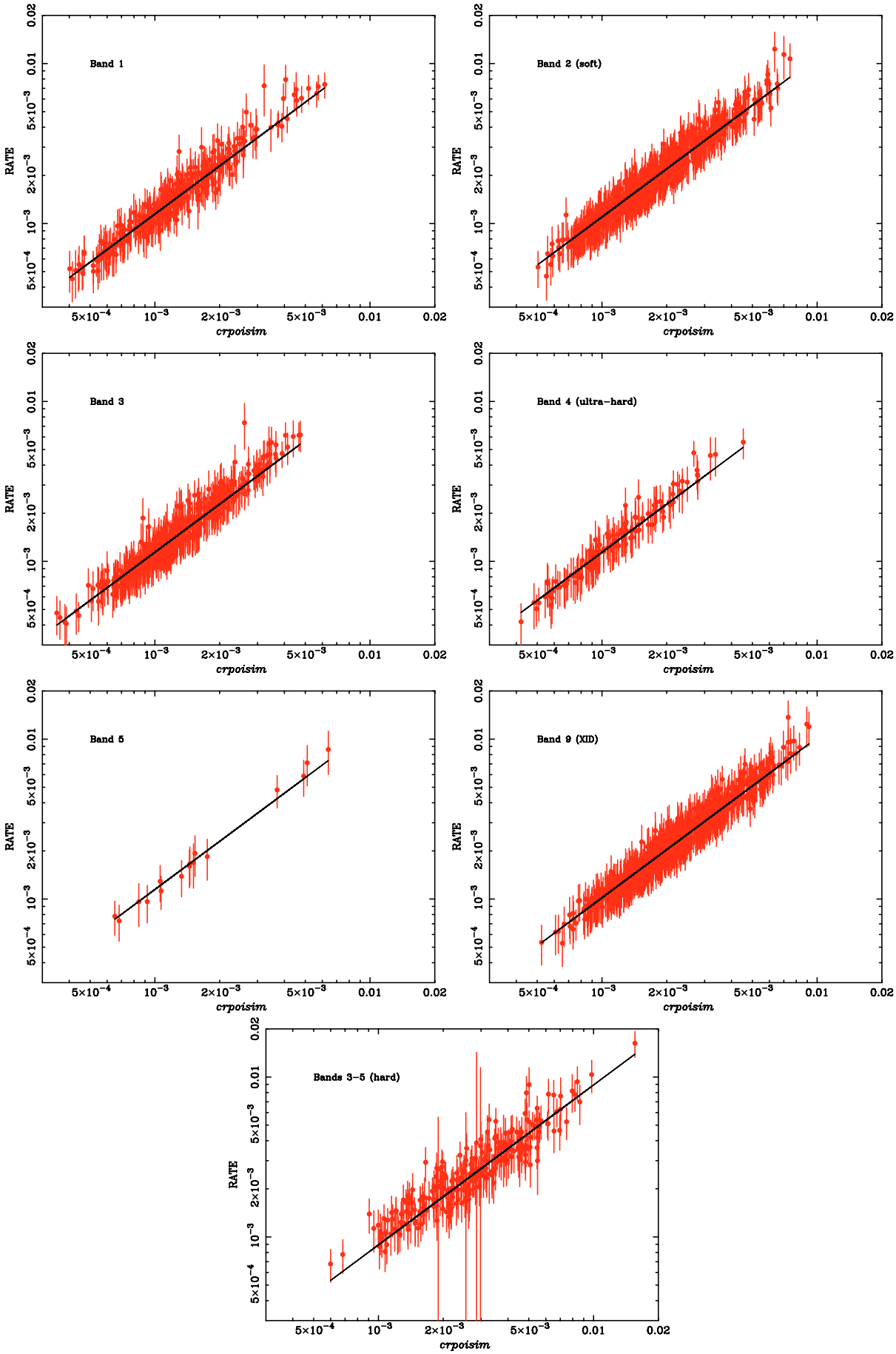

Fig. A.1. RATE vs. *crpoisim* for all bands. Also shown are the best linear fits.

Table B.1. Empirical relationship between the observed errors on the count rates, ΔCR, and the naive $\sqrt{CR/T_{\rm exp}}$. We give the parameters a and b of a linear relation $\Delta CR = a \times \sqrt{CR/T_{\rm exp}} + b$.

band	a	b
2	1.597	-
3	1.419	3.824×10^{-5}
4	1.452	6.166×10^{-5}
5	2.350	1.184×10^{-4}

Table B.2, showing that any internal deviations are small, (<0.1), and that there are no obvious biases for sources selected in different bands. We have repeated the simulations for $\Gamma \equiv 1.8$ and $\Gamma \equiv 1.7$ with similar results and conclusions.

We have also performed an external check against the single power law fits to the "properly" extracted spectra produced by Mateos et al. (2005). In that work the fits were done using `xspec` with response matrices and effective areas generated for each source with the corresponding SAS tasks. Since the Mateos et al. (2005) spectra were extracted between 0.2 and ∼12 keV we have fitted our sources using bands 2, 3, 4 and 5. In Fig. B.1 we show their best fit single power law slopes vs. our best fit slopes for the common accepted sources (a total of 1143 sources which includes some sources fitted by Mateos et al. but not included in their paper, Mateos private communication). The best χ^2 fit proportionality constant using errors in both the X and Y axis is 0.980±0.003. This result makes us confident in our fitting method and shows that we haven't missed significant effects that were not already corrected in the `emldetect` count rates. A number of sources deviate appreciably from the 1:1 relation in Fig. B.1, the effect being more noticeable to the eye for values of $\Gamma_{0.2-12\,\rm keV}$ between about 1.7 and 3. Within that interval the number of sources with $\Gamma_{0.5-10\,\rm keV} > 3$ is only 14% of the corresponding total number of sources. This simple test already indicates that the number of sources with pathological spectral fits is a small minority. We will discuss the influence of these sources in more detail below. We show in Fig. B.2 our best fit slopes versus our 0.5–12 keV count rates. There are some sources with very steep fitted slopes (because they have only been significantly detected in one band), but the bulk of our sources have reasonably "standard" spectral slopes with no significant trends towards too steep or too faint slopes at lower count rates.

Individually the fits are therefore good but we have also assessed whether there are significant biases in the average slope and whether the error bars on the slopes are adequate. We have first studied the distribution of the differences between the slopes divided by the quadratic sum of the errors (which would be expected to follow a $N(0, 1)$ distribution in the Gaussian case). There is a small bias in these "normalised" differences of ∼20% of the combined error bar (in the sense of our results having steeper slopes than Mateos et al.), with a significant dispersion above the expected value. Fitting a Gaussian to this distribution (which is not a Gaussian) finds a similar central value but a much smaller dispersion, indicating that much of the excess variance is due to a limited number of significant outliers.

Assuming Gaussian statistics the error on the mean can be obtained by dividing the standard deviation by the square root of the number of sources (∼1000 in our case). If we perform this calculation for our normalised differences the value is much smaller than the ∼20% relative bias above, which means that the bias is significant (many times the "error on the mean") despite its low relative value.

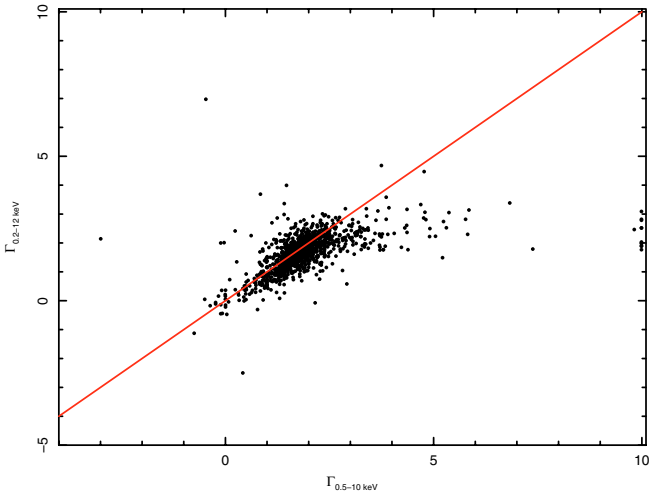

Fig. B.1. Full band power-law slope from Mateos et al. (2005) vs. our 0.5–10 keV slope for the common accepted sources. The solid line shows the 1:1 relation.

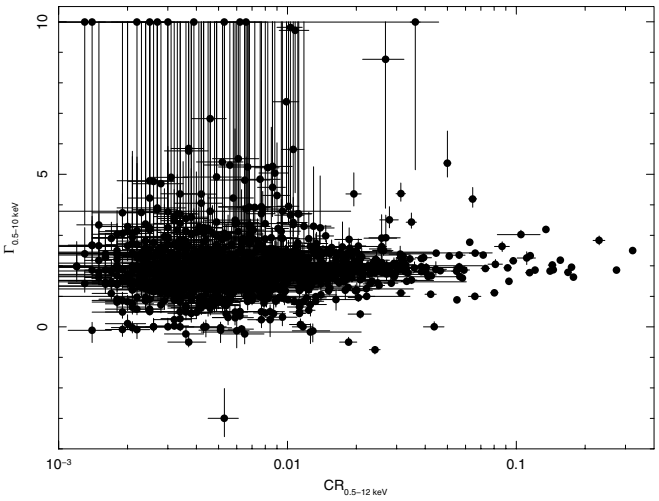

Fig. B.2. Our 0.5–10 keV slope versus the 0.5 to 12 count rate for the 1433 sources in our sample.

Studying the distribution of the absolute differences between the slopes (without dividing by the combined error bar), again there is a bias towards softer slopes in our sample of $\Delta\Gamma \sim 0.12$, with a very significant dispersion which again is much reduced in the Gaussian fit. Our conclusion is therefore similar to above. If we compare our weighted average slopes with Mateos et al there is also a difference, but in the sense of our slopes being flatter than theirs. Since the weighted average essentially discards the sources with large error bars, this means that some of the outliers discussed above are soft sources with large error bars which bias the arithmetic average towards softer slopes.

Table B.2. Number of sources selected in different bands N, weighted average slopes $\langle\Gamma\rangle$, errors (taking into account both the error bars in the individual Γ and the dispersion around the mean) and the number of sources used in the average $N_{\rm ave}$ for the simulated sources (see Section 3). The soft, hard, XID and ultra-hard bands are as defined in the text. "Soft and hard" refers to sources selected simultaneously in the soft and hard bands, "Only soft" refers to sources selected in the soft band but not in the hard band and "Only hard" refers to sources selected in the hard band and not in the soft band

		0.5–4.5 keV		2–10 keV	
Selection	N	$N_{\rm ave}$	$\langle\Gamma\rangle$	$N_{\rm ave}$	$\langle\Gamma\rangle$
Soft	1267	1267	2.008 ± 0.004	1259	2.029 ± 0.007
Hard	397	397	2.008 ± 0.005	396	2.039 ± 0.010
XID	1359	1359	2.007 ± 0.004	1352	2.030 ± 0.007
Ultra-hard	91	91	2.014 ± 0.008	91	2.019 ± 0.013
Soft and hard	345	345	2.009 ± 0.005	345	2.038 ± 0.010
Only soft	922	922	2.007 ± 0.006	914	2.005 ± 0.013
Only hard	52	52	1.99 ± 0.03	51	2.10 ± 0.05